

1 An Emerging Aerosol Climatology via Remote Sensing over Metro Manila, Philippines

2
3 Genevieve Rose Lorenzo^{1,2}, Avelino F. Arellano¹, Maria Obiminda Cambaliza^{2,3}, Christopher
4 Castro¹, Melliza Templonuevo Cruz^{2,4}, Larry Di Girolamo⁵, Glenn Franco Gacal², Miguel
5 Ricardo A. Hilario¹, Nofel Lagrosas⁶, Hans Jarett Ong², James Bernard Simpas^{2,3}, Sherdon Niño
6 Uy², and Armin Sorooshian^{1,7}

7
8 ¹Department of Hydrology and Atmospheric Sciences, University of Arizona, Tucson, Arizona,
9 85721, USA

10 ²Air Quality Dynamics-Instrumentation & Technology Development Laboratory, Manila
11 Observatory, Quezon City, 1108, Philippines

12 ³Department of Physics, School of Science and Engineering, Ateneo de Manila University,
13 Quezon City, 1108, Philippines

14 ⁴Institute of Environmental Science and Meteorology, University of the Philippines, Diliman,
15 Quezon City, 1101, Philippines

16 ⁵Department of Atmospheric Science, University of Illinois, Urbana-Champlain, Illinois, 61801,
17 USA

18 ⁶Center for Environmental Remote Sensing, Chiba University, Chiba, 263-8522, Japan

19 ⁷Department of Chemical and Environmental Engineering, University of Arizona, Tucson,
20 Arizona, 85721, USA

21
22 *Correspondence to:* armin@arizona.edu

23 **Abstract**

24 Aerosol particles in Southeast Asia are challenging to characterize due to their complex life cycle
25 within the diverse topography and weather in the region. An emerging aerosol climatology was
26 established based on AERONET data (December 2009 to October 2018) for clear sky days in
27 Metro Manila, Philippines. Aerosol optical depth (AOD) values were highest from August to
28 October, partly from fine urban aerosol particles, including soot, coinciding with the burning
29 season in Insular Southeast Asia when smoke is often transported to Metro Manila during the
30 southwest monsoon. Clustering of AERONET volume size distributions (VSD) resulted in five
31 aerosol particle sources based on the position and magnitude of their peaks in the VSD and the
32 contributions of specific particle species to AOD per cluster based on MERRA-2. The clustering
33 showed that the majority of aerosol particles above Metro Manila were from a clean marine
34 source (58%), which could be related to AOD values there being relatively smaller than in other
35 cities in the region. The following are the other particle sources over Metro Manila: fine polluted
36 (20%), mixed dust (12%), urban/industrial (5%), and cloud processing (5%). Furthermore,
37 MERRA-2 AOD data over Southeast Asia were analyzed using empirical orthogonal functions.
38 Along with AOD fractional compositional contributions and wind regimes, four dominant
39 aerosol particle air masses emerged: two sulfate air masses from East Asia, an organic carbon
40 source from Indonesia, and a sulfate source from the Philippines. Knowing the local and regional
41 aerosol particle air masses that impact Metro Manila is useful in identifying the sources while
42 gaining insight on how aerosol particles are affected by long-range transport and their impact on
43 regional weather.

44 1. Introduction

45 Although Southeast Asia is one of the most rapidly developing regions in the world with a
46 growing number of extensive research conducted (Reid et al., 2023), there remain knowledge
47 gaps related to aerosol particles in the area (Tsay et al., 2013; Lee et al., 2018; Chen et al., 2020;
48 Amnuaylojaroen, 2023). The region represents a complex geographic, meteorological, and
49 hydrological environment making it challenging to understand aerosol particle characteristics,
50 especially interactions between aerosol particles with their environment (Reid et al., 2013). The
51 island of Luzon in the Philippines in particular is very populated and is characterized by high
52 levels of anthropogenic emissions superimposed on natural emissions from the surrounding
53 waters (AzadiAghdam et al., 2019) and long-range transport of emissions from areas such as
54 Indonesia and East Asia (Braun et al., 2020; Hilario et al., 2020a; Hilario et al., 2020b; Hilario et
55 al., 2021a). Aerosol particle lifecycle in the region is impacted by Philippine weather that is
56 marked by two distinct monsoons, typhoons, the intertropical convergent zone, and impacts from
57 El Niño-Southern Oscillation and Madden-Julian Oscillation (Cruz et al., 2013; Xian et al., 2013;
58 Reid et al., 2012; Reid et al., 2015; Hilario et al., 2021b). Studying this area is informative owing
59 to the wide dynamic range in aerosol particle and weather conditions, which are interconnected.
60 The overlapping of large fraction of cirrus clouds with lower clouds in the area (Hong and Di
61 Girolamo, 2020) makes space-borne remote sensing of aerosol particles very challenging (Reid
62 et al., 2013; Lin et al., 2014). These reasons motivated the NASA Cloud, Aerosol, and Monsoon
63 Processes Philippines Experiment (CAMP²Ex) airborne measurement campaign in 2019 to
64 understand the interaction between tropical meteorology and aerosol particles (Di Girolamo et
65 al., 2015; Reid et al., 2023). However, those short terms measurements cannot provide an
66 adequate assessment of aerosol behavior across all seasons and over many years.

67 The NASA AErosol RObotic NETwork (AERONET) (Holben et al., 1998) is pivotal in
68 providing broad temporal coverage of aerosol characteristics in specific locations with a column-
69 based perspective from the ground up. Aerosol climatology studies in different regions have
70 proved beneficial to understand temporal characteristics of aerosol particle concentrations and
71 properties, in addition to identifying potential source regions along with interactions with clouds
72 and rainfall (Stevens and Feingold, 2009; Li et al., 2011; Tao et al., 2012; Crosbie et al., 2014;
73 Kumar et al., 2015; Alizadeh-Choobari and Gharaylou, 2017; Mora et al., 2017; Aldhaif et al.,
74 2021). To our knowledge, there has not been a remote sensing-based aerosol climatology study
75 for the Metro Manila region of Luzon, which has approximately 16 cities, a population of 12.88
76 million, and a high population density of 20,800 km⁻² (PSA, 2016; Alas et al., 2018).

77 Most of the past studies involving long-term remotely sensed aerosol particle data in Southeast
78 Asia (Cohen, 2014; Nakata et al., 2018; Nguyen et al., 2019b) had no specific focus on the
79 Philippines. The Philippines is considered as part of the Maritime Continent (MC), the island
80 nations sub-region of Southeast Asia. The other Southeast Asia sub-region, Peninsular Southeast
81 Asia (PSEA), comprises those nations within the continental Asia land mass. These two regions
82 have separate aerosol sources and climate, where MC is dependent on the intertropical
83 convergent zone (ITCZ) and PSEA is dependent on both the ITCZ and monsoon systems (Dong
84 and Fu, 2015). Only the southern part of the Philippines is climatologically part of MC (Ramage,
85 1971), however, and northwest Philippines, where Metro Manila is located, is affected by the
86 monsoons and tropical cyclones aside from the ITCZ (Chang et al., 2005; Yumul Jr et al., 2010;
87 Bagtasa, 2017). These unique meteorological influences and extensive local aerosol particle

88 sources warrant a unique aerosol climatology over Metro Manila, one of a polluted source in a
 89 tropical marine environment, and its effects on cloud formation in the area. Aerosol effects on
 90 clouds in the marine environment are associated with the largest uncertainties in climate change
 91 research (Hendrickson et al., 2021; Wall et al., 2022) and the Philippines was ranked as the 5th
 92 country globally as most at risk to climate change and extreme weather from 1997 to 2018
 93 (Eckstein et al., 2018). There have been several surface measurements of aerosol particles made
 94 in Metro Manila for the past 20 years (Oanh et al., 2006; Bautista VII et al., 2014; Cruz et al.,
 95 2019) but columnar ground-based measurements there are just beginning to be established
 96 (Dorado et al., 2001; Ong et al., 2016; Cruz et al., 2023). The AERONET sun photometer is one
 97 of the first long-term column-based aerosol instruments in Metro Manila and the Philippines
 98 (Ong et al., 2016).

99 The goal of this study is to use multi-year AERONET data in Manila Observatory along with
 100 other complementary datasets (MERRA-2, PERSIANN, MISR, HYSPLIT, and NAAPS) to
 101 address the following questions: (1) what are the monthly characteristics of aerosol particles over
 102 Metro Manila, Philippines?; (2) what are the possible sources and factors influencing the
 103 observed characteristics?; (3) what relationships are evident between aerosol particles and cloud
 104 characteristics?; and (4) what are the regional and local aerosol particle air masses that influence
 105 Metro Manila?

106

107 2. Methods

108 This work relies on analysis of several datasets summarized in Table 1 and the following
 109 subsections. The common time range used for all datasets is between January 2009 and October
 110 2018.

111 **Table 1:** Summary of datasets over Metro Manila used in this work covering the period from
 112 January 2009 to October 2018.

Parameter	Data Source	Spatial Coverage	Time Coverage
Aerosol Optical Depth (500 nm)	AERONET	14.635°N, 121.078°E	Jan 2009 - Oct 2018
Asymmetry Factor (440 nm - 1020 nm)	AERONET	14.635°N, 121.078°E	Jan 2009 - Oct 2018
Extinction Angstrom Exponent (440 nm - 870 nm)	AERONET	14.635°N, 121.078°E	Jan 2009 - Oct 2018
Fine Mode Fraction	AERONET	14.635°N, 121.078°E	Jan 2009 - Oct 2018
Precipitable Water	AERONET	14.635°N, 121.078°E	Jan 2009 - Oct 2018
Single Scattering Albedo (440 nm - 1020 nm)	AERONET	14.635°N, 121.078°E	Jan 2009 - Oct 2018
Refractive Index (Real and Imaginary; 440 nm - 1020 nm)	AERONET	14.635°N, 121.078°E	Jan 2009 - Oct 2018
Volume Size Distribution	AERONET	14.635°N, 121.078°E	Jan 2009 - Oct 2018
Low Cloud Fraction (MODIS)	MERRA-2	14.3°N - 14.8°N, 120.75°E - 121.25°E	Jan 2009 - Dec 2018
Planetary Boundary Layer Height	MERRA-2	14.3°N - 14.8°N, 120.75°E - 121.25°E	Jan 2009 - Dec 2018
Relative Humidity (975 mb)	MERRA-2	14.3°N - 14.8°N, 120.75°E - 121.25°E	Jan 2009 - Dec 2018
Sea Level Pressure	MERRA-2	14.3°N - 14.8°N, 120.75°E - 121.25°E	Jan 2009 - Dec 2018
Temperature (975 mb)	MERRA-2	14.3°N - 14.8°N, 120.75°E - 121.25°E	Jan 2009 - Dec 2018
Wind (975 mb)	MERRA-2	14.3°N - 14.8°N, 120.75°E - 121.25°E	Jan 2009 - Dec 2018
Total Extinction Aerosol Optical Depth (550 nm)	MERRA-2	14.3°N - 14.8°N, 120.75°E - 121.25°E	Jan 2009 - Dec 2018

Sulfate, Black Carbon, Organic Carbon, Dust, and Sea Salt Extinction Aerosol Optical Depth (550 nm)	MERRA-2	14.3°N - 14.8°N, 120.75°E - 121.25°E	Jan 2009 - Dec 2018
Precipitation	PERSIANN	14.3°N - 14.8°N, 120.75°E - 121.25°E	Jan 2009 - Dec 2018

113 2.1 Datasets

114 2.1.1 AERONET

115 The central dataset used is that of sun photometer measurements and derived (inversion)
116 parameters from the AERONET (Holben et al., 1998) site at the Manila Observatory in Quezon
117 City, Philippines (14.64°N, 121.08°E, ~70 m. a. s. l.). Direct sunlight extinction measurements
118 were made at nominal wavelengths of 340, 380, 440, 500, 675, 870, 940, and 1020 nm, from
119 which aerosol optical depth (AOD) was calculated (except for 940 nm, which is for water vapor)
120 (Eck et al., 2013). AOD is a commonly used proxy for aerosol particle loading in the air column
121 from the ground up (Holben et al., 2001); higher AOD translates to more aerosol particle
122 extinction in the column above a location. The extinction angstrom exponent (EAE) and the fine
123 mode fraction (FMF) are also AERONET direct sun products that are retrieved after the
124 application of a spectral de-convolution algorithm (O'Neill et al., 2003). For the inversion
125 products, it is through radiative retrievals that the volume size distribution (VSD) and complex
126 refractive index (RI) are gathered and from which single scattering albedo (SSA) and asymmetry
127 factor (AF) are calculated. The AERONET observations were made during clear sky conditions,
128 which has been shown (Hong and Di Girolamo, 2022) to be able to represent all sky conditions.

129 For the inversions, four wavelengths (440, 670, 870, and 1020 nm) of the radiometer spectral
130 channels were chosen for diffuse radiance measurements and to avoid gas absorption (Dubovik
131 et al., 1998). Version 3 Direct Sun and Inversion algorithms (AERONET, 2019; Giles et al.,
132 2019) were used with the Almuqantar Sky Scan Scenario to derive the following parameters with
133 level 2.0 (automatically cloud-cleared and quality controlled datasets with pre- and post-field
134 calibrations) data quality: column AOD (500 nm), fine mode fraction (500 nm), extinction
135 angstrom exponent (440 – 870 nm), precipitable water (940 nm), single scattering albedo (440,
136 670, 870, and 1020 nm), asymmetry factor (440, 670, 870, and 1020 nm), refractive index (440,
137 670, 870, and 1020 nm), and VSD. The version 3 products are able to keep fine mode aerosol
138 particle data (haze and smoke) as well as remove optically thin cirrus clouds in order to retain
139 more aerosol particle measurements in the database (Giles et al., 2019). Cloud screening in the
140 version 3 product improves remote sensing measurements in Southeast Asia in general, where
141 cirrus clouds are pervasive (Reid et al., 2013). At most, a total of 29,037 direct sun and 1419
142 inversion AERONET daytime data points were available between January 2009 and October
143 2018.

144 2.1.2 MERRA-2

145 Modern Era-Retrospective Analysis for Research and Applications, Version 2 (MERRA-2: 0.5°
146 × 0.625° approximate resolution) meteorological and aerosol particle composition reanalysis data
147 (Bosilovich, 2016; Gelaro et al., 2017; Randles et al., 2017) were acquired for the area around
148 Manila Observatory (14.25°N – 14.75°N, 120.9375°E – 121.5625°E). The aerosol reanalysis
149 data includes data assimilation of AOD from the Moderate Resolution Imaging
150 Spectroradiometer (MODIS: Terra, 2000 to present and Aqua, 2002 to present), Advanced Very
151 High Resolution Radiometer (AVHRR, 1979-2002), and Multiangle Imaging SpectroRadiometer
152 (MISR, 2000-2014) (Bucharth et al., 2017; Rizza et al., 2019). The following products were used:

153 M2I3NPASM Assimilated Meteorological Fields (3-hourly) for 975 mb level winds, temperature,
154 relative humidity, and sea level pressure; M2T1NXFLX Surface Flux Diagnostics (1-hourly
155 from 00:30 UTC time-averaged) 2D for planetary boundary layer height; M2T1NXCSP COSP
156 Satellite Simulator (1-hourly from 00:30 UTC time-averaged) for MODIS mean low cloud
157 fraction (cloud top pressure > 680 hPa); and M2T1NXAER Aerosol Diagnostics (1-hourly from
158 00:30 UTC time-averaged) for Total AOD and speciated AOD (Sulfate, Black Carbon (BC),
159 Organic Carbon (OC), Dust, and Sea Salt).

160 MERRA-2 meteorological and aerosol particle composition monthly mean reanalysis data
161 (Bosilovich, 2016; Gelaro et al., 2017; Randles et al., 2017) were also acquired for a larger
162 region ($30^\circ \times 30^\circ$), the Southeast Asia region ($0^\circ\text{N} - 30^\circ\text{N}$, $105^\circ\text{E} - 135^\circ\text{E}$) for the period from
163 2009 to 2018. This is within the spatial domain of the CAMP²Ex airborne measurement
164 campaign which, as mentioned earlier, targets the interaction between tropical meteorology and
165 aerosol particles. The following datasets (0.5° latitude and 0.625° longitude resolution) were
166 used: MERRA-2 `tavgM_2d_aer_Nx`: Aerosol Assimilation (M2TMNXAER) for Total 500 nm
167 AOD and speciated 500 nm AOD (Sulfate, BC, OC, Dust, and Sea Salt) and MERRA-2
168 `instM_3d_ana_Np`: Analyzed Meteorological Fields (M2IMNPANA) for 1000 hPa and 725 hPa
169 level U and V winds. The total MERRA-2 AOD for the region was used along with MISR AOD
170 data to assess the influence of long-range sources to the aerosol column over Manila Observatory.
171 The monthly meteorological and aerosol particle composition data for the region will be used for
172 empirical orthogonal functions, which will be described later.

173 2.1.3 PERSIANN

174 Hourly precipitation data were obtained from the Precipitation Estimation from the Remotely
175 Sensed Information using Artificial Neural Networks (PERSIANN) (Nguyen et al., 2019a)
176 database of the Center for Hydrometeorology and Remote Sensing (CHRS) at the University of
177 California, Irvine (UCI). Hourly data were accumulated for running three-day totals, which were
178 compared to AERONET data. The data were averaged between the four grids that included the
179 area of interest as well as ensuring a similar spatial domain ($14.5^\circ\text{N} - 15.0^\circ\text{N}$, $120.75^\circ\text{E} -$
180 121.25°E) to the MERRA-2 dataset.

181 2.1.4 MISR

182 Monthly 500 nm AOD data (Level 3 Global Aerosol: $0.5^\circ \times 0.5^\circ$ spatial resolution) from 2009 to
183 2018 are used from the Multi-angle Imaging SpectroRadiometer (MISR), (Diner et al., 2007;
184 Garay et al., 2018) as regional (Southeast Asia) baseline remote sensing data to support the
185 Manila Observatory AERONET data. The regional ($30^\circ \times 30^\circ$) MISR data was used to confirm
186 regional sources of aerosols that may be influencing the AOD over Metro Manila. Level 3 MISR
187 products are global maps of parameters available in Level 2 (measurements derived from the
188 instrument data) products. MISR is ideal for remote sensing in the CAMP²Ex region because it
189 has an overpass at 10:30 AM ECT (descending mode) (when cirrus is minimal) and its retrievals
190 have been shown to be unimpacted by small cumulus (Zhao et al., 2009), which are typical in the
191 region. MISR has relatively more accurate AOD and agrees better with AERONET data
192 compared to other satellite products due to its multi-angle measurements (Choi et al., 2019;
193 Kuttippurath and Raj, 2021). The MISR sampling noise is relatively small due to the large
194 domain and seasonal averages that are considered in this study. MISR is also the only passive
195 sensor that speciates aerosol particle size and shape. All these factors led to the choice of using
196 regional MISR data to associate long-range sources influencing AERONET data in Manila

197 Observatory. Monthly mean AOD (bin 0) were extracted for Southeast Asia (0.25°N – 30.25°N,
198 104.75°E – 134.75°E) within the CAMP²Ex region. Monthly mean AOD values were then
199 calculated for each 0.5° grid point and then for the 30° × 30° region, where the standard error in
200 the monthly mean for the region is less than 0.002. MISR monthly mean time series of size,
201 shape, and absorption speciated 550 nm AOD and angstrom exponent in the CAMP²Ex domain
202 (6.5°N – 22.5°N, 116.5°E – 128.5°E; March 2000 to December 2020) are also used to support
203 the findings from the AERONET data.

204 2.1.5 NAAPS

205 Archived maps of total and speciated optical depths and surface concentrations of sulfate, dust,
206 and smoke for Southeast Asia are used from the Navy Aerosol Analysis and Prediction System
207 (NAAPS: 1° × 1° spatial resolution) (Lynch et al., 2016), and which are publicly available at
208 <https://www.nrlmry.navy.mil/aerosol/>. This reanalysis product relies on the Navy Global
209 Environmental Model (NAVGEM) for meteorological fields (Hogan et al., 2014). Hourly maps
210 were downloaded for aerosol particle events of interest based on AERONET data. These maps
211 help associate possible regional emission sources to extreme aerosol loading events in Manila
212 Observatory.

213 2.1.6 HYSPLIT

214 Back-trajectories from the National Oceanic and Atmospheric Administration’s (NOAA) Hybrid
215 Single-Particle Lagrangian Integrated Trajectory (HYSPLIT) model (Stein et al., 2015; Rolph et
216 al., 2017) were used to provide support for the AERONET monthly aerosol characteristics and
217 the chosen case studies. Three and seven-day back-trajectories with six-hour resolution were
218 generated based on the NCEP/NCAR reanalysis meteorological dataset and with a resolution of
219 1° and a vertical wind setting of “model vertical velocity”. The three-day data were used to map
220 the density of trajectories reaching Manila Observatory in each month from 2008 to 2019. The
221 seven-day data were used in the analysis of the case studies. Trajectories were computed for an
222 end point with an altitude of 500 m above ground level at the Manila Observatory. This altitude
223 represents the mixed layer based on related surface air quality studies (Crosbie et al., 2014; Mora
224 et al., 2017; Schlosser et al., 2017; Aldhaif et al., 2020), including a previous study for the same
225 area (Stahl et al., 2020).

226 2.1.7 NASA Worldview

227 Archived maps of cloud fraction (Aqua MODIS and Terra MODIS) over Metro Manila and
228 Southeast Asia were downloaded from NASA Worldview (<https://worldview.earthdata.nasa.gov>)
229 for events of interest based on AERONET data.

230

231 **2.2 Clustering**

232 Available AERONET VSD data (0.050 μm to 15.000 μm particle radius in 22 logarithmically
233 equidistant discrete points, 1419 data points) were clustered via k-means clustering (Lloyd,
234 1982). The algorithm used was k-means++ (Arthur and Vassilvitskii, 2006). The ideal number
235 of clusters was chosen based on relatively highest (>0.5) average silhouette value and the
236 presence of a cluster with a second peak in the larger accumulation mode of the VSD. The
237 clusters were analyzed based on their associated meteorological conditions and aerosol particle
238 characteristics and were classified into air mass types (Table 2) based on estimates from previous
239 studies (Dubovik et al., 2002; Pace et al., 2006; Kaskaoutis et al., 2007; Kaskaoutis et al., 2009;
240 Sorooshian et al., 2013; Kumar et al., 2014; Sharma et al., 2014; Che et al., 2015; Kumar et al.,

241 2015; Deep et al., 2021). The first four mentioned air mass types in Table 2 are the most general,
 242 and four more classifications based on aerosol particle sources are included. The urban/industrial
 243 air mass type here refers to local combustion along with long-range transported biomass burning
 244 (Kaskaoutis et al., 2009). While these classifications are not rigid definitions of air masses, they
 245 help in understanding the sources that contribute to aerosols in Metro Manila and in identifying
 246 cases where certain sources are more influential than others.

247 **Table 2:** Summary of threshold values of aerosol optical depth (AOD), angstrom exponent (AE),
 248 fine mode fraction (FMF), and single scattering albedo (SSA) used to identify air mass types.

Air Mass Type	AOD	AE	FMF	SSA	Source
Clean Fine	< 0.1 ^a	> 1 ^a	> 0.7 ^a	-	Sorooshian et al., 2013
Polluted Fine	> 0.1 ^a	> 1 ^a	> 0.7 ^a	-	Sorooshian et al., 2013
Clean Coarse	< 0.1 ^a	< 1 ^a	< 0.3 ^a	-	Sorooshian et al., 2013
Polluted Coarse	> 0.1 ^a	< 1 ^a	< 0.3 ^a	-	Sorooshian et al., 2013
Clean Marine	< 0.2 ^b	< 0.9 ^d	-	0.98 ^e	Kaskaoutis et al., 2009 Dubovik et al., 2002
Urban/Industrial	> 0.2 ^b	> 1 ^d	-	0.9- 0.98 ^e	Kaskaoutis et al., 2009 Dubovik et al., 2002
Biomass Burning	-	> 1.4 ^a	-	0.89- 0.95 ^e	Deep et al., 2021 Dubovik et al., 2002
Desert Dust	> 0.3 ^c	< 1 ^d	-	0.92- 0.93 ^e	Kaskaoutis et al., 2009 Deep et al., 2021 Dubovik et al., 2002

^a from MODIS

^c AOD at 400 nm

^e SSA at 440 nm

^b AOD at 500 nm

^d AE at 380 nm to 870 nm

249

250 **2.3 Extreme Event Analysis**

251 Aerosol particle events based on the three clusters with the highest VSD concentrations were
 252 identified to characterize different types of sources and processes impacting aerosol particle
 253 columnar properties above Metro Manila. The three events are described below.

254 2.3.1 Smoke Long Range Transport

255 Events related to transported biomass burning/smoke were chosen from the AERONET VSD
 256 data that were clustered as urban/industrial (with a dominant submicrometer peak) (Eck et al.,
 257 1999) over Metro Manila. Cases with the highest black carbon contribution to total AOD from
 258 the MERRA-2 dataset were considered. Maps from NAAPS of high smoke contributions to
 259 AOD and surface smoke contributions in the direction of back-trajectories HYSPLIT were used
 260 to provide support for the likely source and transport pathway for the smoke cases.

261 2.3.2 Dust Long Range Transport

262 A dust transport case over Metro Manila was identified from the AERONET VSD dust cluster
 263 (with an enhanced coarse peak in the AERONET VSD compared to the submicrometer fraction)

264 (Eck et al., 1999), the highest dust contribution to AOD from the MERRA-2 dataset, and high
265 dust contributions to AOD from NAAPS. Surface dust concentrations from NAAPS along the
266 HYSPLIT back-trajectories improved the plausibility of dust for this case.

267 2.3.3 Cloud Processing

268 Cloud processing events were identified based on bimodal submicrometer VSDs (Eck et al.,
269 2012) and a relatively large sulfate contribution to AOD over Metro Manila from the MERRA-2
270 dataset, since this species is predominantly produced via cloud processing (Barth et al., 2000;
271 Faloon, 2009). The presence of clouds was verified qualitatively with MODIS (Aqua and Terra)
272 imagery from NASA Worldview in the path of air parcels reaching Metro Manila based on
273 HYSPLIT back-trajectories.

274

275 **2.4 Empirical Orthogonal Functions**

276 Regional analysis of aerosol particles in Southeast Asia and Asia in general show the prevalence
277 of biomass burning in the region, as well as the larger influence of anthropogenic emissions in
278 East Asia (Nakata et al., 2018). These large prevalent sources may overshadow other relevant but
279 weaker sources in the region, such as local sources. Due to the complex nature of aerosol
280 particles, analysis techniques such as principal component analysis and clustering along with
281 recent improvements in gridded datasets help detect spatial and temporal patterns that would
282 otherwise be difficult to make with noise interference and even weak signals (Li et al., 2013;
283 Sullivan et al., 2017; Plymale et al., 2021). Understanding the dominant air masses around
284 Southeast Asia will help in distinguishing local and transported particles that influence the
285 aerosol climatology in Metro Manila.

286 To contextualize the analysis of aerosol particle masses in Metro Manila, major regional sources
287 of aerosol particles in Southeast Asia were identified based on the dominant principal
288 components from empirical orthogonal (EOF) analysis of AOD. EOF analysis was done on the
289 monthly AOD data (January 2009 to December 2018) from MERRA-2 for the Southeast Asia
290 region for the months similar in scope to the AERONET data. EOF analysis needs a complete
291 dataset with no data gaps, which is not available with pure satellite retrievals like MISR; the
292 MERRA-2 reanalysis dataset alleviates this issue.

293 The monthly MERRA-2 AOD maps ($0^\circ - 30^\circ\text{N}$, $105^\circ\text{E} - 135^\circ\text{E}$ with 0.5° latitude and 0.625°
294 longitude resolution) (Lat: 61 rows x Lon: 49 columns) for the Southeast Asia region (presented
295 subsequently) were first deseasonalized. Then, the AOD anomaly per grid per year (of the 120
296 months) was calculated by subtracting the monthly mean AOD from each value of a given month
297 (Li et al., 2013). The anomalies per grid were weighted depending on their latitude by
298 multiplying the anomalies by the square root of the cosine of their latitudes.

299 EOF, specifically singular value decomposition (SVD), analysis (Björnsson and Venegas, 1997)
300 was then performed. To prepare the data for the analysis, they were transformed such that the
301 final matrix was a 2D matrix (120 x 2989) with each row representing a year, and each column
302 representing a grid in the map. The matrix was analyzed for eigenvalues using SVD in Matlab,
303 which outputs the eigenvalue (S) and eigenvector (U: principal components and V: empirical
304 orthogonal functions) matrices. The eigenvalues were, by default, arranged in descending order.

305 Each PC time series was standardized by dividing each PC value by the standard deviation per
306 PC time series (120 months).

307 An eigenvalue spectrum was also plotted based on the variance explained by each eigenvalue
308 and error bars that were calculated using the North test (North et al., 1982). Then, the
309 unweighted AOD anomalies were regressed onto the first three standardized PCs. Each grid
310 therefore had a regression between 120 pairs (unweighted AOD anomalies vs standardized PCs).
311 From the linear regression equation, the regression coefficient per grid was calculated. Each grid
312 on the Southeast Asia map was colored based on the calculated regression coefficient value.

313

314 **2.5 Correlations**

315 The first three standardized PCs of AOD anomalies were correlated to deseasonalized
316 compositional AOD fractions (Sulfate, BC, OC, Dust, and Sea Salt). For each correlation, the t-
317 test value was calculated, and the resulting t-score was compared to a t-critical value for ~n= 100
318 pairs (n is the number of pairs of data, in this case 120 months) for 0.90 confidence level, which
319 is 1.660. Correlations that have t-values exceeding +1.660 or less than -1.660 (two-tailed test) are
320 significant (90% confidence).

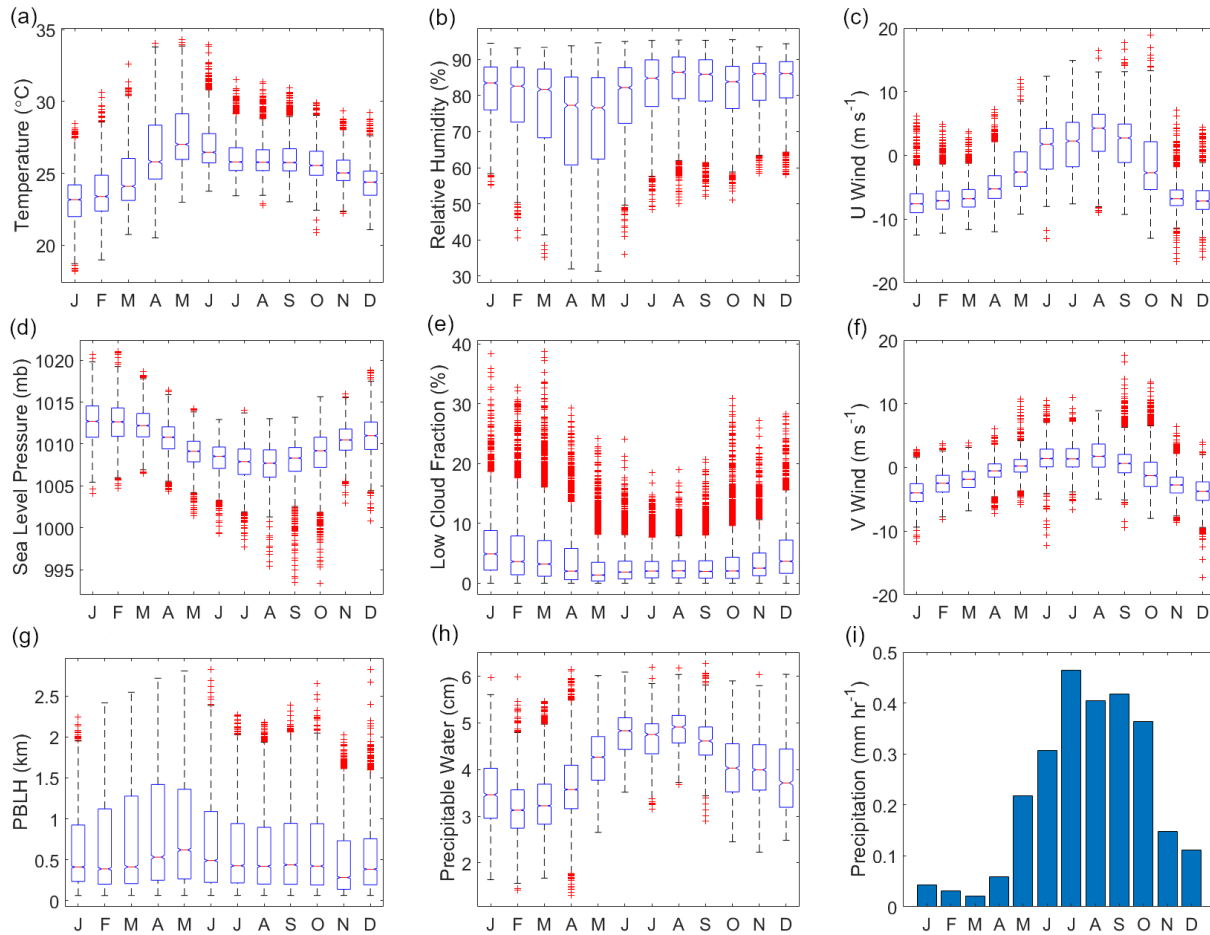
321

322 **3 Results and Discussion**

323 **3.1 Meteorology and Atmospheric Circulation**

324 Knowledge of monthly behavior of weather in the study region helps interpretation of aerosol
325 particle data. Philippine climate is influenced both by the winter northeast monsoon
326 (~November to April, Amihan) and the summer southwest monsoon (~May to October, Habagat)
327 (Coronas, 1920; Flores, 1969; Matsumoto et al., 2020). Median 3-hourly temperatures at 975 mb
328 per month (MERRA-2, 975 mb) (Fig. 1a) ranged from 23.2 °C in January during the winter
329 northeast monsoon, to 27.0 °C in May during the transition from the summer season, as defined
330 in (Bañares et al., 2021), to the southwest monsoon. May was also the month with the lowest
331 median 3-hourly relative humidity (76.6%) (MERRA-2, 975 mb) (Fig. 1b). The highest median
332 level of relative humidity at 975 mb for a month was in August (86.5 %) during the summer
333 southwest monsoon, which is also the time of the year (June to August) when rainfall peaks in
334 the region where the sampling station (Manila Observatory) is located (Coronas, 1920; Cruz et
335 al., 2013). The highest mean hourly precipitation (Fig. 1i) per month was from July (0.46 mm hr⁻¹)
336 to September (0.42 mm hr⁻¹), while March exhibited the lowest mean hourly rainfall (0.02 mm
337 hr⁻¹). Like relative humidity and precipitation, median precipitable water (from available
338 AERONET data of 513 points in August, 4015 points in February, and 5049 points in March)
339 (Fig. 1h) was highest in August (4.9 cm) and lowest in February and March (3.1 cm and 3.2 cm,
340 respectively).

341



342

343

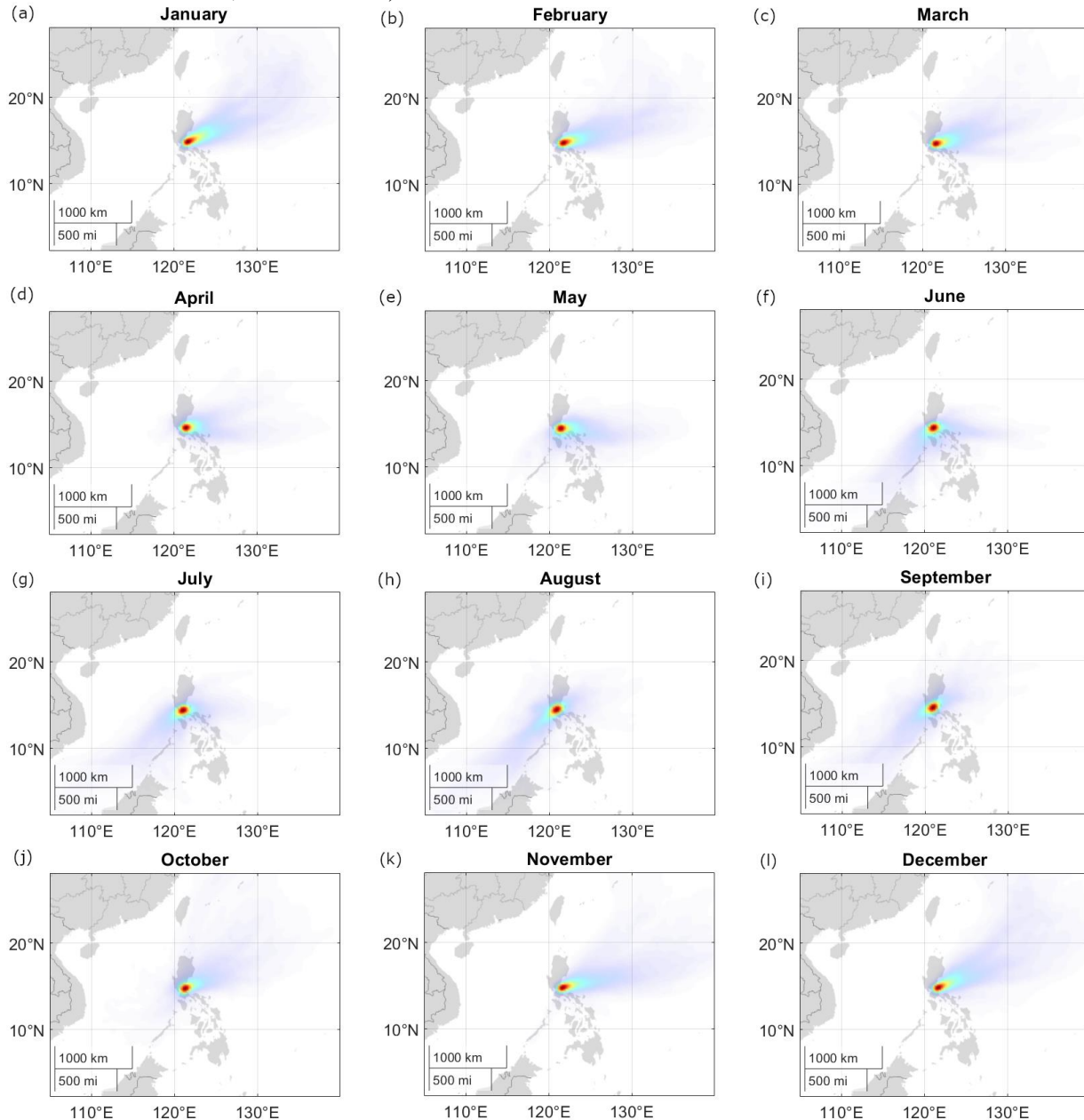
344 **Figure 1:** Monthly characteristics of meteorological parameters for Metro Manila, Philippines
 345 based on data between January 2009 and October 2018. MERRA-2 parameters: (a) temperature
 346 at 975 mb, (b) relative humidity at 975 mb, (c/f) u and v wind at 975 mb, (d) sea level pressure,
 347 (g) planetary boundary layer height (PBLH), (e) low cloud fraction (cloud top pressure > 680
 348 hPa); AERONET: (h) precipitable water (data counts per month Jan: 2131, Feb: 4015, Mar:
 349 5049, Apr: 5844, May: 3448, Jun: 1696, Jul: 652, Aug: 513, Sep: 753, Oct: 1700, Nov: 2084,
 350 Dec: 1449); PERSIANN: (i) mean hourly precipitation per month.

351

352 The lowest 3-hourly median pressures (MERRA-2) were observed (Fig. 1d) between July and
 353 September during the southwest monsoon season (~985.2 – 985.8 mb). This is also the time
 354 when the most number of tropical cyclones pass the island of Luzon (Wu and Choy, 2016). The
 355 highest 3-hourly median pressures (988.1 – 990.0 mb) were during the winter northeast
 356 monsoon.

357 Median winds (MERRA-2) were from the south/southwest direction from June to September
 358 (Fig. 1c and 1f), associated with the summer southwesterly monsoon. HYSPLIT back-
 359 trajectories show the same wind pattern (Fig. 2f to 2i). The highest median 3-hourly wind speeds
 360 (MERRA-2) (Fig. 1c and 1f) during the southwest monsoon were recorded for August (u: 4.2 m
 361 s⁻¹ and v: 1.7 m s⁻¹). Median winds begin to transition in October and November (to the northeast

362 monsoon: Amihan) (Fig. 2j and 2k) coming from the east/northeast and maintained until
 363 February (Fig. 2b), which is towards the end of the winter northeast monsoon. There were
 364 generally higher wind speeds and the highest median 3-hourly wind speeds of the year
 365 (MERRA-2) (Fig. 1c and 1d) in January (u: -7.6 m s^{-1} and v: -4.0 m s^{-1}). Median winds shifted
 366 toward a more easterly source from March to May (transition time before the Habagat monsoon)
 367 (Fig. 2c to 2e) accompanied by decreasing median 3-hourly wind speeds (u = -6.8 m s^{-1} , v = -1.9
 368 m s^{-1} to u: -2.6 m s^{-1} , v = 0.2 m s^{-1}).



369 **Figure 2:** Density plots of HYSPLIT trajectories reaching Manila Observatory per month from
 370 2009 to 2018. Red denotes areas with the greatest number of back trajectories within a 100 km
 371 radius. The colors represent density value contributions to Matlab-calculated cumulative
 372 probability distribution surfaces (100 km radius) from coordinates of three-day back trajectories
 373 of the specific months.
 374

375 The transition times between the monsoons (when the wind directions shift and wind speeds
376 change) are also the times of the highest (May, Fig. 1g, 621.2 m) and lowest (November, Fig. 1g,
377 279.6 m) median planetary boundary layer heights (MERRA-2). The median planetary boundary
378 layer height was highest during the period (May) of highest temperatures, lowest relative
379 humidity, reduced air pressure, and lowest monthly median low cloud fraction (MERRA-2) (Fig.
380 1e) (1.4 %). The lowest monthly median planetary boundary layer height was observed during
381 the period (November) when temperatures were beginning to cool and air pressure was rising.
382 The monthly maximum low cloud fraction was lowest in July (18.5 %) during the summer
383 southwest monsoon while the monthly median and monthly maximum low cloud fractions
384 (MERRA-2) (Fig. 1e) were highest (38.3 % max, 4.9 % median) in January during the winter
385 northeast monsoon.

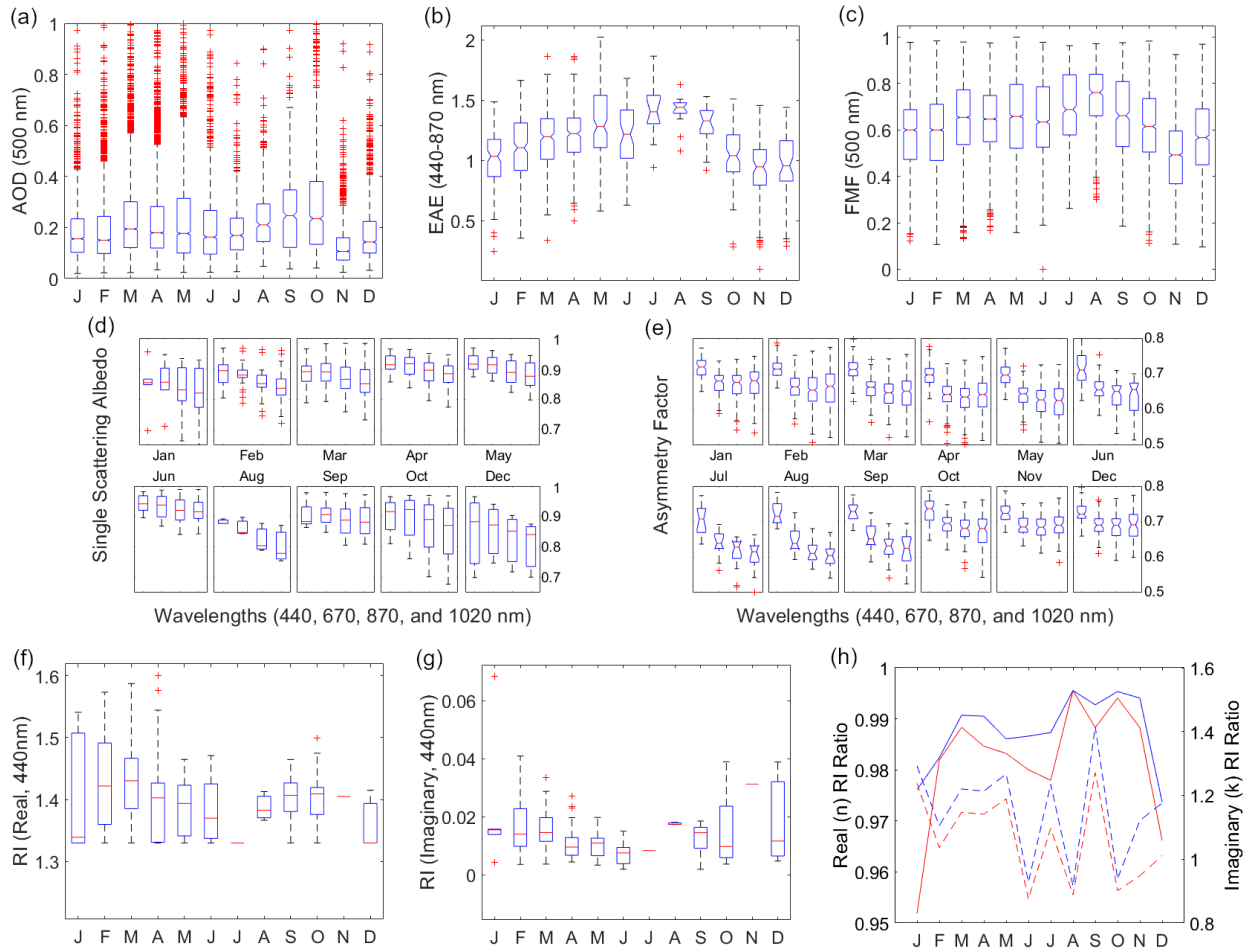
386

387 **3.2 Aerosol Particle Characteristics**

388 3.2.1 Aerosol Optical Depth

389 Monthly median AOD (AERONET, 500 nm) (Fig. 3a) over the Manila Observatory was highest
390 from August (0.21) to October (0.23) around the time of the summer monsoon when winds were
391 coming from the southwest (Figs. 2h to 2i) (Holben et al., 2001). This is the same time of year
392 when biomass burning activities occur in the Indonesian region southwest of Metro Manila
393 (Glover and Jessup, 1998; Kiely et al., 2019; Cahyono et al., 2022). Studies have shown that
394 AOD in the Philippines increases during the biomass burning season in Indonesia (Nguyen et al.,
395 2019b; Caido et al., 2022). Regional AOD (550 nm) over the larger Southeast Asia domain from
396 MISR and MERRA-2 (Fig. 4) had a similarly large peak around the same time beginning in
397 September until October which, however, was second only in magnitude to a March peak, which
398 is influenced by biomass burning in Peninsular Southeast Asia (PSEA) (Gautam et al., 2013;
399 Hyer et al., 2013; Dong and Fu, 2015; Wang et al., 2015; Yang et al., 2022). This is consistent
400 with the peak in speciated AOD due to fine (radii $<0.7 \mu\text{m}$), spherical, and absorbing aerosols
401 that were observed by MISR from March to April (Fig. S1). This larger peak in March,
402 attributed to PSEA (which is ~ 2000 km west of the Philippines), was not as prevalent in the
403 AERONET AOD data over Manila Observatory in Metro Manila due to the dominant easterly
404 winds in the Philippines in March (Fig. 2c) and more localized sources.

405

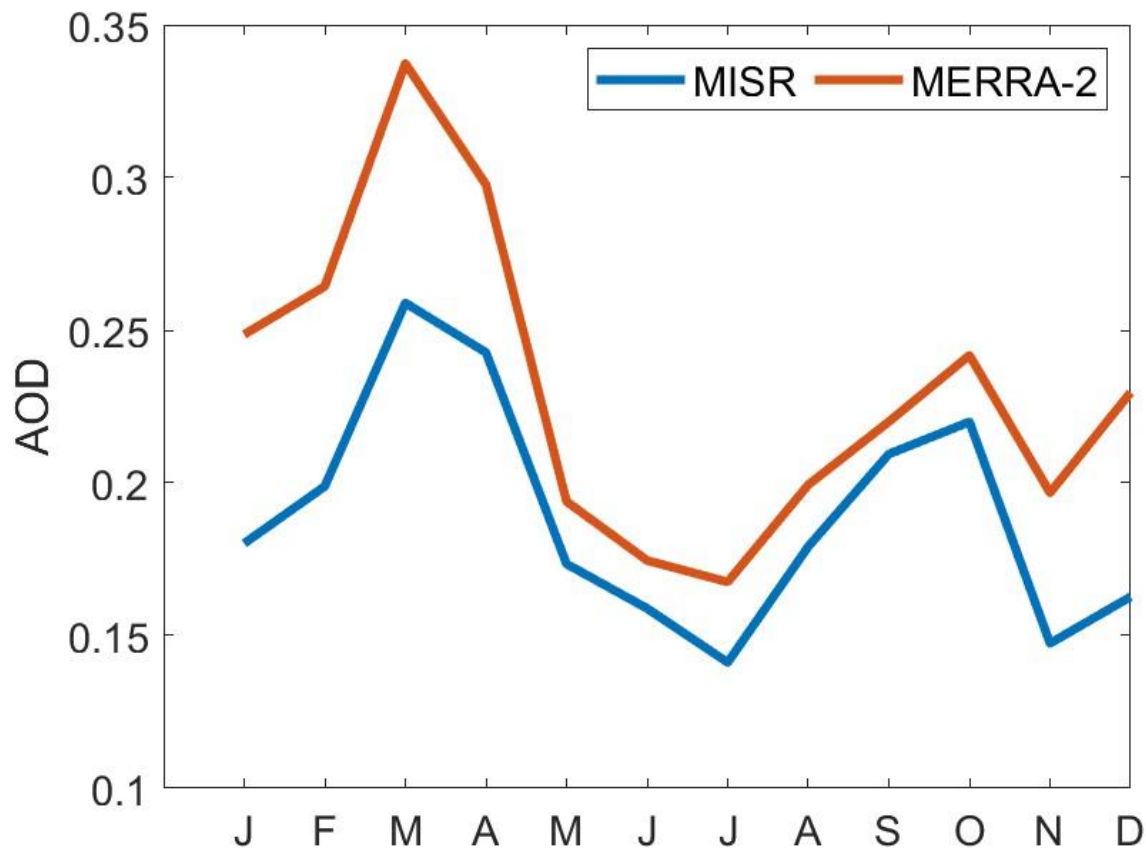


406
 407 **Figure 3:** Monthly characteristics of AERONET aerosol particle parameters: (a) aerosol optical
 408 depth (AOD at 500 nm with y-axis until 1.0 only for larger boxplot resolution) with counts (Jan:
 409 2107, Feb: 3931, Mar: 4923, Apr: 5755, May: 3389, Jun: 1653, Jul: 637, Aug: 483, Sep: 718,
 410 Oct: 1555, Nov: 2001, Dec: 1386), (b) extinction angstrom exponent (EAE at 440-870 nm) with
 411 counts (Jan: 102, Feb: 248, Mar: 312, Apr: 309, May: 137, Jun: 53, Jul: 14, Aug: 18, Sep: 18,
 412 Oct: 79, Nov: 77, Dec: 52), (c) spectral de-convolution algorithm (SDA) retrievals of fine mode
 413 fraction (FMF at 500 nm) with the same counts as AOD, (d) single scattering albedo (SSA) from
 414 440 nm (leftmost boxplot) to 1020 nm (rightmost boxplot) with counts (Jan: 6, Feb: 31, Mar: 62,
 415 Apr: 50, May: 29, Jun: 8, Aug: 3, Sep: 5, Oct: 17, Dec: 3), (e) asymmetry factor (AF) from 440
 416 nm (leftmost boxplot) to 1020 nm (rightmost boxplot) with the same counts as EAE, (f) real and
 417 (g) imaginary refractive index (RI) values (440 nm) with the same counts as SSA, and (h)
 418 refractive index ratios (where the blue line is the ratio of RI at 440 nm and 670 nm, the red line is
 419 the ratio of RI at 440 nm and the average RI for the 675–1020 nm wavelengths, and the broken
 420 lines are the imaginary refractive index ratios) for Metro Manila, Philippines based on data
 421 between January 2009 and October 2018.

422 There is a notable dip in the monthly median AERONET AOD over Manila Observatory from
 423 the peak in October to the lowest monthly median AOD (0.11) in November (Fig. 3a), just
 424 slightly above defined background levels (<0.1) (Holben et al., 2001), when the windspeeds
 425 were picking up and were coming from the east to northeast directions (Fig. 2k) in the direction
 426 of the Philippine Sea and the West Pacific Ocean. This dip was also observed in the regional

427 (30° × 30°) AOD data (MISR and MERRA-2, Fig. 4). This is most probably due to the decrease
 428 in the AOD contribution from fine (radii <0.7 μm) and spherical particles based on size speciated
 429 MISR AOD (Fig. S1). Larger and non-spherical particle contributions to AOD increase in
 430 November in the Southeast Asia region. The MERRA-2 AOD is relatively higher than the MISR
 431 AOD probably due to assimilation of MODIS data into MERRA-2. Studies in Asia (Xiao et al.,
 432 2009; Qi et al., 2013; Choi et al., 2019) have observed relatively higher MODIS AOD compared
 433 to MISR AOD.

434



435

436 **Figure 4:** Monthly mean AOD (550 nm) in Southeast Asia (30° × 30°) from 2009 to 2018 from
 437 MISR (blue line) and MERRA-2 (red line).

438 There were 338 instances (~1.2 % of the time based on the total number of 28,538 valid
 439 AERONET AOD data points) of AOD values exceeding 1, indicative of heavy aerosol particle
 440 loading (Huang et al., 2021). Because AOD is extrinsic (it depends on mass), AOD describes
 441 total aerosol particle loading and we examine other aerosol particle parameters from AERONET
 442 to make more informed inferences about size and composition.

443 3.2.2 Extinction Angstrom Exponent and Fine Mode Fraction

444 The extinction angstrom exponent (EAE) relates the extinction of light at specific wavelengths
445 and is indicative of aerosol particle size (Ångström, 1929). The EAE is usually greater for
446 smaller particles (~4 for very small particles that undergo Rayleigh scattering, > 2 for small
447 particles, < 1 for large particles like sea salt and dust, and 0 for particles as large as cloud drops)
448 (Schuster et al., 2006; Bergstrom et al., 2007). The highest monthly median EAE (Fig. 3b) from
449 2009 to 2018 over the Manila Observatory was observed from July (~1.4) to September (~1.3),
450 during the southwest monsoon. This period is associated with the biomass burning southwest of
451 the Philippines (Oanh et al., 2018; Stahl et al., 2021; Crosbie et al., 2022). The median (per
452 month) EAE ranged from ~0.9 in November to ~1.4 in August, a range which is within the
453 values from previous studies collected from mixed sites and urban/industrial areas with both fine
454 and coarse particles (Eck et al., 2005; Giles et al., 2012). The high EAE over Manila Observatory
455 from July to September is probably regional in nature based on the MISR data showing increased
456 EAE with increased AOD from fine, spherical, and absorptive particles (Fig. S1) in Southeast
457 Asia during the same months.

458 EAE increases with AOD (Fig. S2), which means that the greater particle loading is contributed
459 by smaller particles (Smirnov et al., 2002). Of the high loading cases (AOD >1) over Manila
460 Observatory, the EAE values were mostly greater than 0.8 indicating fine mode particles (Che et
461 al., 2015). The EAE values in August were the highest compared to other months including
462 having the highest minimum value of any month (0.71) (Fig. S2), due to smaller particles (~EAE
463 >1 for fine particles, Table 2). The lowest EAE values (0.08) and thus the largest particles were
464 observed in December, which again may be regional in nature with MISR EAE also lowest
465 during this time with increased AOD from larger and non-spherical particles (Fig. S1).

466 The fine mode fraction (FMF) describes the prevalence of fine mode particles in the column of
467 air above the surface. The fine mode fraction (Fig. 3c) from 2009 to 2018 was highest in August
468 (monthly median of 0.75) and lowest in November (monthly median of 0.45). This is consistent
469 with the EAE values discussed earlier with the prevalence of smaller particles in August and
470 larger particles in November. In August (Fig. 2h) the southwest monsoon is known to coincide
471 with the transporting of fine smoke particles to Luzon. In November (Fig. 2k), the prevalent
472 winds may have already shifted to easterly (Matsumoto et al., 2020) implying more marine-
473 related sources associated with coarser particles.

474 3.2.3 Single Scattering Albedo

475 The single scattering albedo (SSA) is the most important aerosol particle parameter determining
476 whether aerosol particles will have a warming or cooling effect (Reid et al., 1998). SSA is the
477 ratio of the scattering coefficient to the total extinction (scattering and absorption) coefficient
478 (Bohren and Clothiaux, 2006) of aerosol particles. Higher SSAs are related to more reflective
479 aerosol particles while more absorbing aerosol particles will have lower SSA values; values
480 range from 1 (reflective) to 0 (absorbing). Monthly median SSA values were largest in June
481 (0.94 at 440 nm), suggesting the presence of more reflective aerosol particles, and smallest in
482 August (0.88 at 440 nm and 0.78 at 1020 nm) suggesting more absorptive particles that are
483 similar in range to the SSA of biomass burning particles (Table 2). August is when biomass
484 burning is prevalent to the southwest of the Philippines and associated with soot particles that are
485 absorptive.

486 The sensitivity of SSA to different wavelengths depends on the type of aerosol particles present.
487 More specifically, aerosol particle size and refractive index (which is related to aerosol particle
488 composition) both affect the SSA (Dubovik and King, 2000; Bergstrom et al., 2007; Moosmüller
489 and Sorensen, 2018). For dust-type particles, SSA increases with wavelength because of lower
490 dust absorption in the higher visible to infrared wavelengths (Dubovik et al., 2002), while for
491 urban particles (including black carbon), which absorb light at longer wavelengths, SSA
492 decreases with wavelength (Reid et al., 1998; Bergstrom et al., 2002). The presence of organic
493 carbon may affect this spectral dependence; however, because organic particles absorb in the
494 UV, this lowers SSA at wavelengths shorter than 440 nm (Kirchstetter et al., 2004). Monthly
495 median SSA generally decreased with increasing wavelength for all months with available data
496 (Fig. 3d) presumably due to the influence of more urban particles in contrast to dust.
497 Noteworthy though are the monsoon transition months of April, September, and October (Fig.
498 3d), which had increased SSA from 440 nm to 670 nm, possibly from organics along with black
499 carbon due to transported smoke. The back-trajectories for these months (Figs. 2d, 2i, and 2j)
500 suggest sources from the northeast that are closer to Luzon during these months compared to
501 other months. This indicates the possibility of more local sources. Increasing the certainty of
502 sources associated with aerosol particles necessitates looking at other available aerosol particle
503 parameters, discussed subsequently.

504 3.2.4 Asymmetry Factor

505 The asymmetry factor quantifies the direction of scattering of light due to aerosol particles, with
506 values ranging from -1 (back scatter) to 0 (uniform scattering) to 1 (forward scatter). It is
507 important in modeling climate forcing because it affects the vertical distribution of the radiation
508 in the atmosphere (Kudo et al., 2016; Zhao et al., 2018). The asymmetry factor is dependent on
509 particle size, shape, and composition and the value of 0.7 is used in radiative models (Pandolfi et
510 al., 2018).

511 Lower asymmetry factors are related to smaller particles (at constant AOD) (Bi et al., 2014).
512 Measured values due to biomass burning, for example, are 0.54 (550 nm) in Brazil (Ross et al.,
513 1998) and 0.45 – 0.53 (550 nm and including dust) over central India (Jose et al., 2016). There
514 have been relatively higher values observed in western, central, and eastern Europe (0.57 – 0.61
515 at 520 – 550 nm) (Pandolfi et al., 2018) and the U.S. East Coast (0.7 at 550 nm) (Hartley and
516 Hobbs, 2001). In Norway, the asymmetry factor for background summer conditions was 0.62
517 and was higher in the springtime at 0.81 (862 nm) during Arctic haze events (Herber et al.,
518 2002). Highest values are associated with dust such as those measured in the Sahara being 0.72 –
519 0.73 (500 nm) (Formenti et al., 2000). Over Metro Manila, the asymmetry factors from the
520 AERONET data at the 675, 870, and 1020 nm were similar across months (Fig. 3e). The monthly
521 median asymmetry factors at 440 nm ranged from 0.70 (April and May) to 0.74 (October), while
522 for 670, 870, and 1020 nm the monthly median asymmetry factors were smaller and ranged from
523 0.62 – 0.69. These values were closely related to those observed over the U.S. East Coast as
524 mentioned earlier, perhaps due to the proximity of the location to the coast (10 km east of Manila
525 Bay and 100 km west of the Philippine Sea) as well as its location in Manila, which is a large
526 local source due mostly to vehicles (Cruz et al., 2019).

527 The monthly median asymmetry factor in Metro Manila was greatest towards the end of the year
528 (October to December) for all the wavelengths, suggesting larger particles when winds (Figs. 2j
529 to 2l) come from the Philippine Sea in the northeast. It was in March and April that the monthly

530 median asymmetry factor was minimal for 440 nm and in August for 670, 870, and 1020 nm.
531 These were the times when aerosol particles were smallest. March to April represents the driest
532 time of the year in Manila (Fig. 1b and 1h) perhaps preventing particle growth and where the
533 local sources may be dominating, even as back-trajectories (Fig. 2c and 2d) extend all the way
534 from the Philippine Sea to the east. This is corroborated by results from other studies showing
535 that the asymmetry factor seems to be enhanced by relative humidity (Zhao et al., 2018). The
536 unexpected low asymmetry factor values in August, however, are probably because of the source
537 of the particles. August had the highest relative humidity and precipitable water (Fig. 1b and 1h)
538 but is also when the back-trajectories (Fig. 2h) were from the southwest, possibly affected by the
539 Indonesia fires, which could have transported more non-hygroscopic fine particles.

540 Fine particles have been observed to exhibit decreasing asymmetry factors with increasing
541 wavelength (Bergstrom et al., 2003). This trend is observed in all the months for the monthly
542 median asymmetry factors (Fig. 3e) suggesting the predominance of smaller aerosol particles.
543 The greatest decrease in the asymmetry factor (all wavelengths) was in August, consistent with
544 the lowest observed values of the year (670, 870, and 1020 nm). Transported biomass burning
545 particles are the probable dominant particles during this time. They are usually composed of
546 hygroscopic inorganics, non-hygroscopic soot, and relative non-hygroscopic organic fractions
547 (Petters et al., 2009). Knowing the composition of biomass burning particles over the study
548 region will help in the understanding of hygroscopicity and its impacts on radiation.

549 3.2.5 Refractive Index

550 Refractive index is an intrinsic parameter as it does not depend on the mass or the size of
551 particles, and thus can be used to infer aerosol particle composition (Schuster et al., 2016). For
552 the case of the AERONET data, which include refractive index values that are insensitive to
553 coarse particles (Sinyuk et al., 2020), the focus of the discussion will be for fine mode particles
554 and may be limited when coarse particles are involved. Refractive index measurements are
555 complex since they include real and imaginary parts related to light scattering and absorption,
556 respectively. All aerosol particles scatter light but only certain types absorb light significantly.
557 The most prominent particle absorbers in the atmosphere are soot carbon, brown carbon (organic
558 carbon that absorbs light), and free iron from dust (hematite and goethite in the ultraviolet to
559 mid-visible) (Schuster et al., 2016). For this study, we examine refractive index values at 440 nm
560 wavelength. Pure sources of soot carbon have the highest real refractive index values (~1.85) as
561 well as the highest imaginary refractive index (~0.71), both independent of wavelength (Koven
562 and Fung, 2006; Van Beelen et al., 2014). Brown carbon and dust have relatively lower real
563 refractive index values at 440 nm (~1.57 and ~1.54) and imaginary refractive index values
564 (~0.063 and ~0.008) that decrease with increasing wavelength (Xie et al., 2017).

565 In this study the range of the monthly median real refractive index values (440 nm) was from
566 1.33 (December and January) to 1.43 (March) (Fig. 3f). Water uptake by aerosol particles
567 decreases the real refractive index values (Xie et al., 2017) and thus the lowered real refractive
568 indices over the Manila Observatory can be due to the presence of more water in the atmosphere
569 in general and/or the increased presence of more hygroscopic particles. December and January
570 are not necessarily the months that have the highest moisture content, but they are months when
571 back-trajectories reaching the column over the Manila Observatory are from the Philippine Sea
572 to the northeast presumably transporting hygroscopic particles. As reported in previous sections,
573 relatively larger particles are observed around this time of the year and thus sea salt can be an

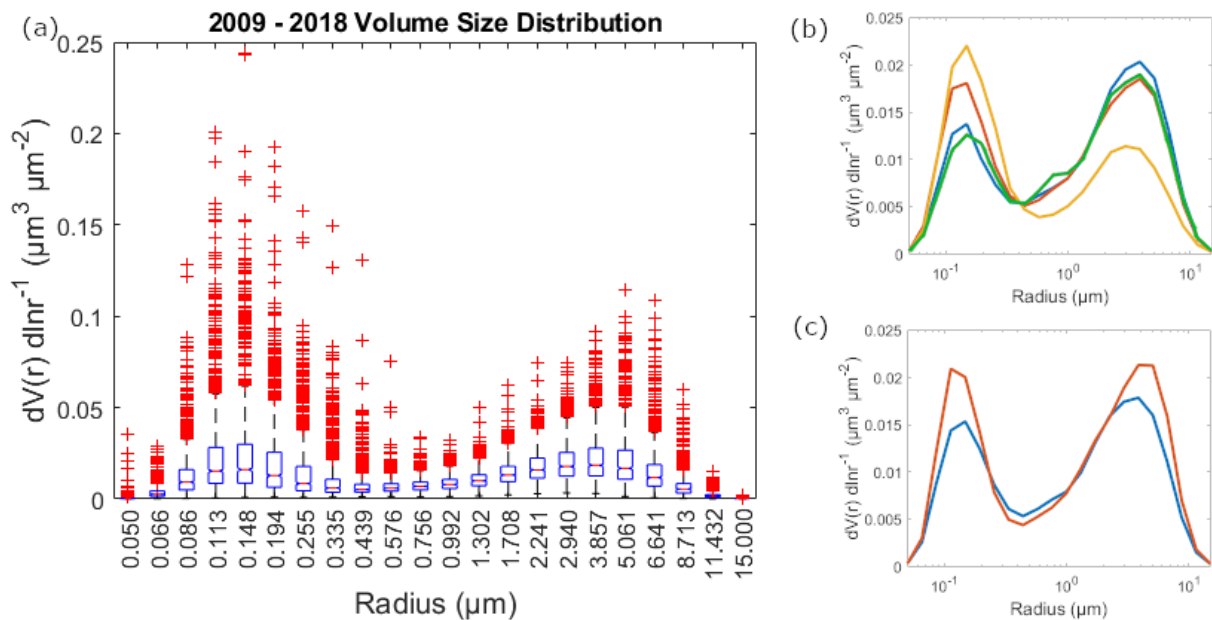
574 important contributor. The greatest change in the monthly median real refractive index with
575 increasing wavelength also was observed in December (Fig. 3h), possibly due the increased
576 fractional contribution of constituents other than soot carbon (because the real refractive index of
577 soot carbon is invariant with wavelength). Noteworthy as well is the month of August (Fig. 3f),
578 which has the smallest range of real refractive index values, possibly indicating a more
579 homogenous aerosol particle source compared to other months. August is the month with the
580 highest relative humidity (Fig. 1b) as well as highest precipitable water (Fig. 1h), while this is
581 also the month when long-range biomass burning emissions are observed to be highest, and
582 when the real refractive index values would otherwise be expected to be highest.

583 Water content seems to play a significant role in the real refractive index values in Manila.
584 March, when the monthly median real refractive index values are highest (Fig. 3f), is when
585 precipitable water vapor (Fig. 1h) is among the lowest in the year. The months around March are
586 also when maximum real refractive indices (1.57 in February, 1.59 in March, and 1.60 in April)
587 were observed (Fig. 3f). March was when there was a relatively small change in real refractive
588 index value with wavelength perhaps related to greater soot carbon fractions during this time,
589 due possibly to the contribution of biomass burning from Peninsular Southeast Asia (Shen et al.,
590 2014). Looking more closely at the imaginary refractive index values will help elucidate this
591 issue.

592 Monthly median imaginary refractive index values (440 nm) ranged from 0.007 in June to 0.015
593 in September and December (Fig. 3g). These are low compared to those of the pure soot carbon
594 mentioned earlier because of the mixed nature of the sampling site with contributions from
595 brown carbon and dust. The highest imaginary refractive index values in September and
596 December suggest the greatest fractional contribution of soot because the highest imaginary
597 refractive index values are associated with soot. These are also similar in magnitude to biomass
598 burning particles in the Amazon (0.013) (Guyon et al., 2003). The key distinction between soot
599 carbon and other major absorbers (brown carbon and dust) is that its imaginary refractive index
600 is invariant with wavelength. Both brown carbon and dust exhibit a decrease in the imaginary
601 refractive index with increasing wavelength (Xie et al., 2017). The ratios of imaginary refractive
602 index values (440 nm to average of 670–1020 nm) (Fig. 3h) show a relative invariance with
603 wavelength (ranging from 0.88 to 1.4), which indicates the dominance of soot as the major
604 absorber in the region (Eck et al., 2003). While observed wavelength invariance points to high
605 soot contributions, the size of the particles can help distinguish between brown carbon, which
606 reside mainly in the fine mode, and dust sources, which yield more coarse particles (Schuster et
607 al., 2016). September is during the southwest monsoon, which is when, as noted in the earlier
608 sections, fine particles were most prevalent. This is also the time when the imaginary refractive
609 index varied most with wavelength (1.4 ratio of the imaginary refractive index at 440 nm and the
610 imaginary refractive index average for 670 nm to 1020 nm in Fig. 3h) possibly with greater
611 absolute contributions from brown carbon, even with the highest soot carbon fractional
612 contributions. Brown carbon has been observed both from primary and aged aerosol particle
613 emissions from biomass burning (Saleh et al., 2013). As noted earlier, December also had the
614 highest imaginary refractive index values as well as relatively coarser particles, possibly due to
615 larger dust absolute contributions even with the highest soot carbon fraction contributions. The
616 lowest monthly median imaginary refractive index values in June, on the other hand, when fine
617 mode particles prevail suggest highest fractional contributions of brown carbon relative to other
618 months (Fig. 3h).

619 3.2.6 Volume Size Distributions

620 The volume size distribution (VSD) is another way to be able to more deeply characterize
 621 aerosol particles, specifically related to their effect on climate, weather, and clouds (Haywood
 622 and Boucher, 2000; Feingold, 2003). In the Manila Observatory dataset, there was a bi-modal
 623 VSD for the entire dataset (Fig. 5a). The fine mode median values peaked in the accumulation
 624 mode at 0.148 μm particle radius while the coarse mode median values peaked at 3.857 μm (Fig.
 625 5a and Table S1). The median coarse mode amplitudes and volume concentrations were higher
 626 than the fine mode amplitudes and volume concentrations for most of the year (DJF, MAM, and
 627 SON, Fig. 5b and Table S1), except during the southwest monsoon (JJA) when the fine mode
 628 amplitude and volume concentration was higher. This is consistent with observations earlier of
 629 fine mode prevalence during the southwest monsoon. Median VSD amplitudes (Fig. 5c) were
 630 greater in the afternoon, with higher peaks and volume concentrations for both the fine and
 631 coarse modes, compared to the morning. There was a slightly larger coarse median amplitude
 632 and volume concentration, compared to the accumulation mode median amplitude and volume
 633 concentration, for both the morning and afternoon size distributions. While the VSDs confirm
 634 several observations based on the analysis of the aerosol particle parameters presented earlier,
 635 not much further information is gained especially regarding chemical composition. Size
 636 distributions are a result of contributions from multiple sources, and thus being able to
 637 discriminate the sources based on their characteristic size distributions will help identify relevant
 638 sources.
 639



640

641 **Figure 5:** (a) VSD results derived from AERONET measurements at Metro Manila between
 642 January 2009 and October 2018. Median VSDs over the study period based on (b) season (blue:
 643 DJF, red: MAM, orange: JJA, green: SON) and (c) time of day (blue: AM, red: PM).

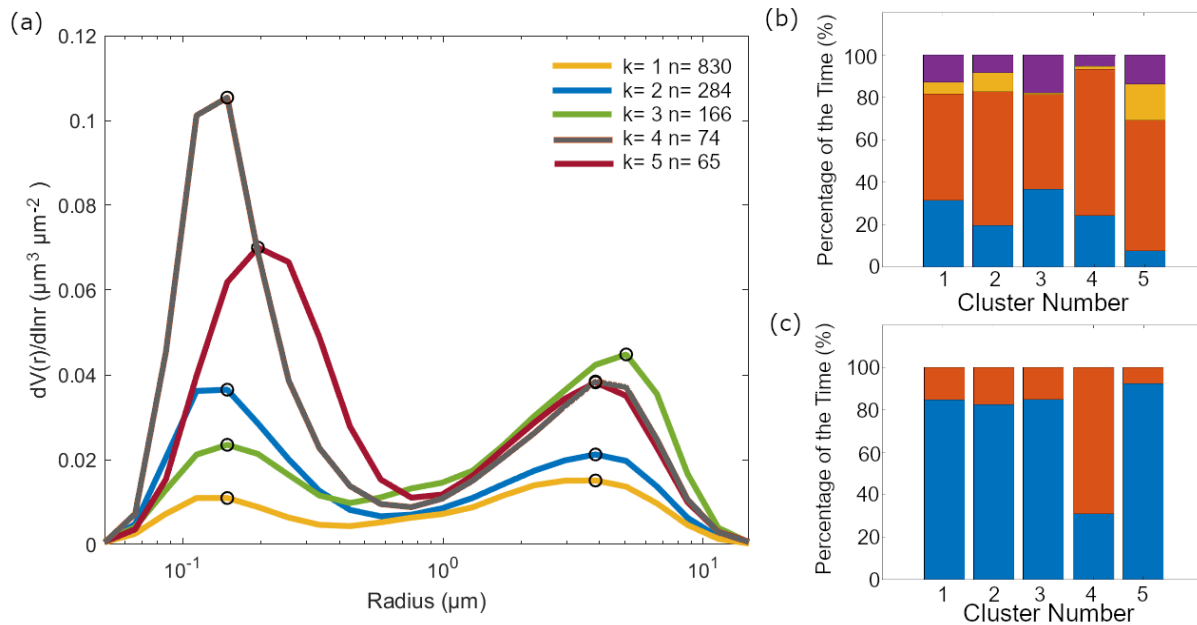
644

645 **3.3 Clusters**

646 3.3.1 VSD Cluster Profiles

647 Five clusters were identified to best represent the VSD (Fig. 6a). The average of the VSDs in
 648 each cluster varied depending on the height of the peaks in the accumulation mode and the
 649 coarse mode. In Metro Manila, the accumulation mode is associated with aged aerosol particles
 650 and combustion (Cruz et al., 2019). The majority of the data (830 count out of 1419 total VSD
 651 profiles) were clustered together in a profile (cluster 1) that had relatively low average
 652 magnitudes of volume concentration for both the accumulation ($0.01 \mu\text{m}^3 \mu\text{m}^{-2}$) and coarse (0.02
 653 $\mu\text{m}^3 \mu\text{m}^{-2}$) modes, with the volume concentration magnitude of the coarse mode peak slightly
 654 higher than the volume concentration magnitude of the accumulation mode peak. The next
 655 prevalent cluster profile (284 counts, cluster 2) had an average fine mode peak for the volume
 656 concentration ($0.04 \mu\text{m}^3 \mu\text{m}^{-2}$) which was more than twice as much than the previous profile but
 657 with a similar coarse mode peak for the volume concentration ($0.02 \mu\text{m}^3 \mu\text{m}^{-2}$). The average
 658 coarse mode peak for the volume concentration ($0.04 \mu\text{m}^3 \mu\text{m}^{-2}$) was the highest (compared to
 659 the four other cluster profiles) for the third prevalent cluster profile (166 counts, cluster 3);
 660 cluster 3 also had a slightly shifted volume concentration peak in the coarse mode to a higher
 661 radius ($5.06 \mu\text{m}$) compared to other clusters. The coarse mode dominated this VSD compared to
 662 other profiles (lower magnitude for the accumulation mode peak for the volume concentration,
 663 $0.02 \mu\text{m}^3 \mu\text{m}^{-2}$). The two remaining cluster profiles exhibited high average magnitudes of
 664 volume concentration in both the accumulation and coarse modes. The fourth prevalent cluster
 665 profile (74 counts, cluster 4) had the highest average absolute magnitude for the volume
 666 concentration in the accumulation mode ($0.11 \mu\text{m}^3 \mu\text{m}^{-2}$), while the fifth prevalent cluster profile
 667 (65 counts, cluster 5) had a slightly smaller accumulation mode peak for the volume
 668 concentration ($0.07 \mu\text{m}^3 \mu\text{m}^{-2}$) that was shifted to a slightly higher radius ($0.19 \mu\text{m}$ compared to
 669 $0.15 \mu\text{m}$). Both clusters 4 and 5 had similar average coarse mode peak volume concentration
 670 magnitudes ($0.04 \mu\text{m}^3 \mu\text{m}^{-2}$).

671



672

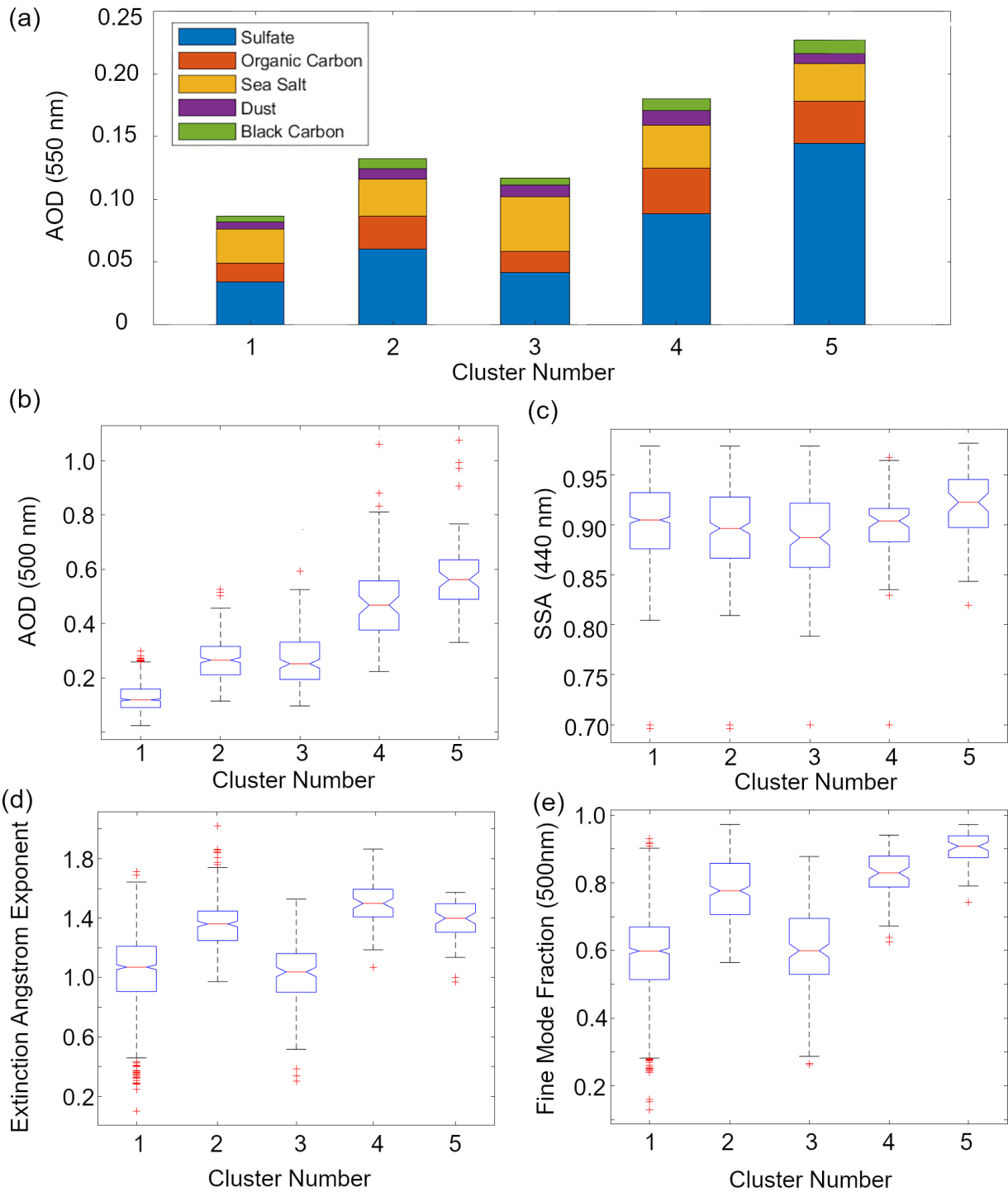
673 **Figure 6:** (a) Cluster analysis of VSD data yielding five characteristic and averaged VSDs with
 674 the number of points per cluster shown in the legend. The black circles on the curves show the

675 peak locations in the submicrometer ($<1 \mu\text{m}$) and coarse ($\geq 1 \mu\text{m}$) modes. The relative abundance
676 of each cluster is shown for different (b) seasons (blue: DJF, red: MAM, orange: JJA, violet:
677 SON) and (c) times of day (blue: AM, red: PM).

678 The clusters were distributed across seasons (Fig. 6b), with clusters 1 and 2 being the most
679 evenly distributed among the clusters. Cluster 3, which had the highest coarse mode peak, had
680 the greatest contribution from September to November compared to other clusters. Cluster 4,
681 which had the highest accumulated mode peak compared to other clusters, had the greatest
682 contribution from March to May as well as to afternoon VSDs compared to other clusters (Fig.
683 6b and 6c). Relative contributions of VSDs from June to August were highest for cluster 5,
684 which had the shifted accumulated mode peak.

685 Median total (AERONET) AOD values (Fig. 7b) were lowest (0.12) for cluster 1, though it had
686 the second highest sea salt fractional contributions (31%) (Fig. 7a) to total AOD (MERRA-2)
687 among all the clusters. Cluster 2 had relatively mid-range median total AOD values (0.27) that,
688 along with clusters 4 and 5, were dominated by sulfate and organic carbon (46% and 20%).
689 Cluster 3 had similar, but slightly lower median total AOD (0.25) compared to cluster 2. Cluster
690 3 was distinct because it had the largest total (0.04) and fractional contribution (37%) from sea
691 salt among all clusters. Clusters 4 and 5 had the highest median total AOD values (0.47 and
692 0.56), with cluster 5 having the highest absolute and fractional sulfate contributions (0.14 and
693 64%) among the clusters. Integrating the above results with their corresponding aerosol particle
694 properties can help associate the clusters to air masses.

695



696
 697 **Figure 7:** (a) Average compositional contributions to aerosol optical depth (AOD at 550 nm)
 698 from MERRA-2 per identified cluster (counts per cluster from 1 to 5: 830, 284, 166, 74, 65).
 699 Boxplots of AERONET (b) total AOD (500 nm), (c) single scattering albedo (SSA at 440 nm),
 700 (d) extinction angstrom exponent (EAE at 440 nm – 870 nm total), and (e) fine mode fraction
 701 (FMF at 500 nm) per cluster.

702
 703 3.3.2 Air Mass Types

704 Air masses have been classified in previous studies based on their AOD, EAE, FMF, and SSA
705 values (e.g., Lee et al., 2010 and Aldhaif et al., 2021). The criteria from different studies (Table
706 2) were applied per cluster. Median total AOD of cluster 1 (0.12) was less than 0.2 (Fig. 7b),
707 which is the threshold for sea salt sources (Kaskaoutis et al., 2009; Kaskaoutis et al., 2007). Half
708 of the data points in cluster 1 also fall below the threshold for clean environments (AOD < 0.1)
709 (Sorooshian et al., 2013). Based on its median EAE (1.07, where EAE < 1 is coarse and EAE > 1
710 is fine) and FMF (0.60) values (Fig. 7d and 7e), cluster 1 is a mixture of fine and coarse
711 particles. The fine Cluster 1 is the only cluster with a median that meets that threshold value for
712 clean marine sources (AOD < 0.2), and we know from Sect. 3.3.1 that its average VSD
713 magnitude was greater for the coarse fraction and that its sea salt contribution to total AOD was
714 second greatest among the clusters. Thus, most probably, cluster 1 is a background clean marine
715 source, since it also is predominant throughout the seasons (Fig. 6b). This makes sense given the
716 proximity of the ocean to Metro Manila from both the east and the west. The median SSA (0.90
717 at 440 nm) for cluster 1 (Fig. 7c), however, suggests the presence of absorbing particles most
718 probably due to high black carbon in the local source (Cruz et al., 2019) that is mixed in with this
719 generally clean marine source.

720 Most of the data from the other clusters all fall in the polluted category (Table 2), based on their
721 median total AODs (>0.1) (Fig. 7b). Cluster 2 has a median FMF value of 0.78 (Fig. 7e), which
722 suggests that most of the particles in this air mass are in the fine fraction. They are, however, not
723 sufficiently dominant in the aerosol for them to be typical of urban/industrial sources. The
724 average VSDs (Fig. 6a) of cluster 2 similarly suggest that their relative accumulation mode
725 magnitude is higher than the coarse magnitude, but not much higher. Like cluster 1, cluster 2 is
726 also more evenly distributed across the seasons (Fig. 6b). The median SSA for cluster 2 (0.90 at
727 440 nm) is also similar to the SSA of cluster 1 (Fig. 7c) where the local and background particles
728 are mixed. Cluster 2 could be a fine polluted background source superimposed on the dominant
729 marine source. Metro Manila is a megacity with continuous and large amounts of sources that
730 could be, due to its proximity to the ocean, interacting with the background.

731 Based on its median EAE value (1.04) (Fig. 7d), cluster 3 is mixed but mostly in the coarse
732 fraction, consistent with its VSD profile (Fig. 6a) which has the highest coarse magnitude (FMF
733 = 0.60) compared to the other clusters. The contribution of data from September to February is
734 greatest in cluster 3, consistent with expected coarser particles during this period when the winds
735 are initially shifting from the southwest before becoming more northeasterly, as previously
736 noted. Median SSA (0.89 at 440 nm) was lowest for cluster 3 (Fig. 7c), this and the relatively
737 high coarse particle contribution suggests cluster 3 as a possible dust source based on past
738 studies (Lee et al., 2010). This air mass can be a mixture of local sources and transported dust air
739 masses, the large sea salt contribution (~37%) to total AOD (Sect. 3.3.1) can be related to long-
740 range transport.

741 Both clusters 4 and 5 have median total FMF (0.83 and 0.91) (Fig. 7e) values exceeding the mark
742 (> 0.8, Table 2) for urban/industrial air masses. Combining this and results from the previous
743 sections confirms that cluster 4 can be an urban/industrial source given that it had the highest
744 median accumulated mode peak and organic carbon contribution (~20%) to total AOD among
745 the clusters. The median SSA for cluster 4 (0.90 at 440 nm) was similar to the median SSA of
746 clusters 1 and 2 (Fig. 7c), but the maximum SSA value for this cluster was lowest in general
747 among all the clusters suggesting cluster 4 has the net most absorptive effect. The cluster 4 air

748 mass is probably from local sources and transported biomass burning emissions. The high
749 median EAE (1.40, Fig. 7d) may be associated with aerosol particles due to biomass burning
750 (Deep et al., 2021).

751 Cluster 5 had the highest median total AOD (0.56) and FMF (0.91) values (Fig. 7b and 7e). It
752 also had the highest sulfate contribution (~64%) to total AOD (Fig. 7a), the highest median SSA
753 (0.92 at 440 nm, thus most reflective particles among the clusters) (Fig. 7c), and a shifted
754 accumulation mode peak (Fig. 6a). These characteristics suggest that cluster 5 is a possible cloud
755 processing air mass (Eck et al., 2012). The larger peak in the accumulation mode is possibly the
756 cloud signature. Previous studies have attributed this larger mode to cloud processing due to the
757 conversion of SO₂ to sulfate (Hoppel et al., 1994). Cloud processing is a major source of sulfate
758 (Barth et al., 2000).

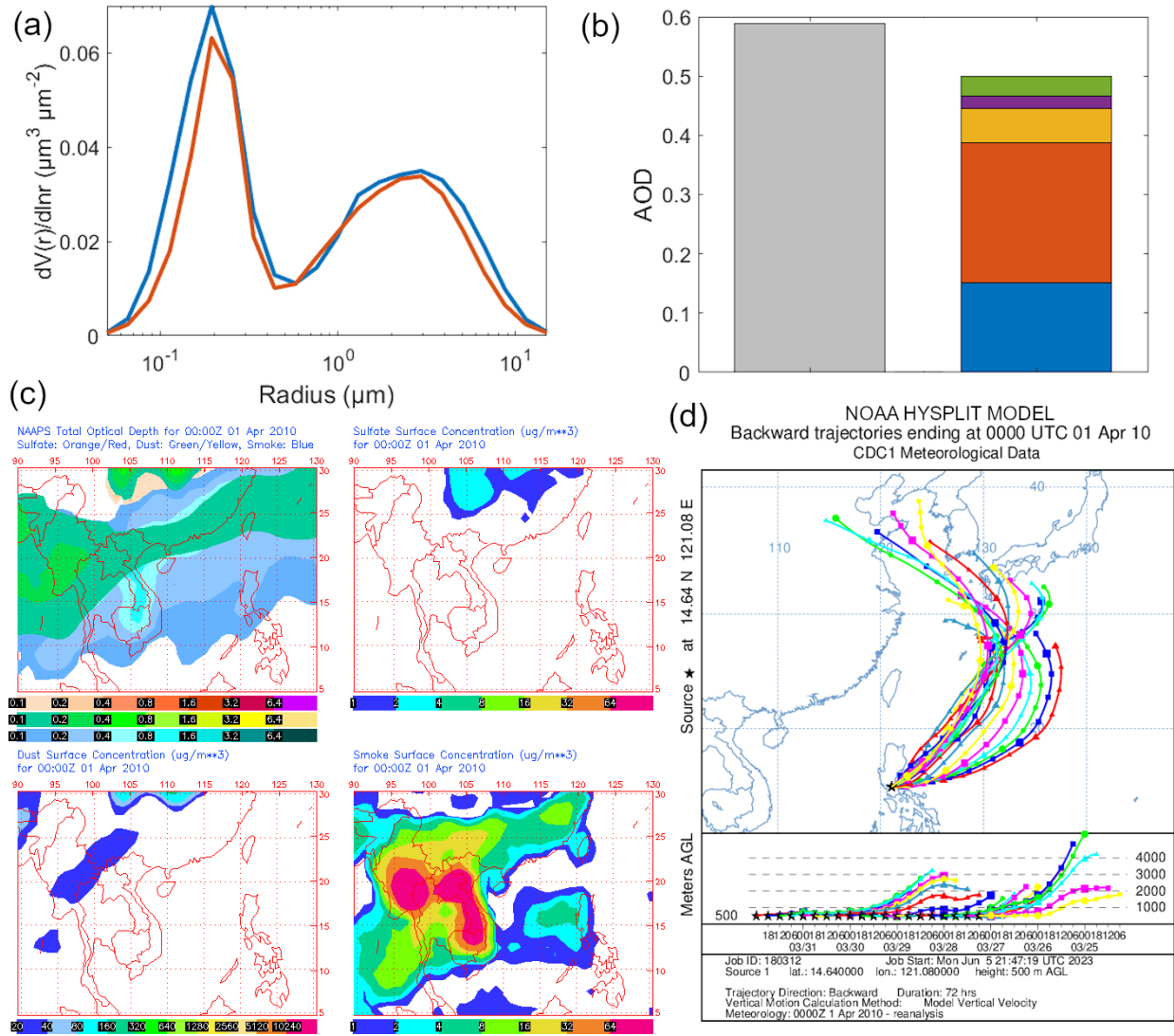
759 The distribution of the air masses based on the abundance of the VSD profiles per cluster suggest
760 prevalent clean marine (58% of the total VSD counts) and background fine polluted (20%) air
761 masses over Metro Manila. The mixed dust (12%), urban/industrial (5%), and cloud processing
762 (5%) air masses contribute 22% altogether. We can investigate more deeply and look at specific
763 case studies that can better describe the air masses identified here.
764

765 **3.4 Case Studies**

766 Selected case studies are used to highlight periods with the highest AOD values and strongest
767 clear sky (no rain and heavy clouds) daytime aerosol particle sources within the sampling period.
768 As such, the clusters that are associated with the selected case studies are the clusters (3-5) with
769 higher VSD concentration magnitudes.
770

771 **3.4.1 Long Range Transport of Smoke**

772 Both cases of long-range transport of smoke discussed below have similar VSDs (Fig. 8a and 9a)
773 to the urban/industrial cluster VSD (cluster 4, Fig. 6a). Organic carbon was the dominant
774 contributor to AOD (Fig. 8b and 9b) for both long-range transport cases. The first of two events
775 occurred around 1 April 2020 with smoke presumed to come from East Asia. The VSD of this
776 specific case (Fig. 8a) is most like the urban/industrial cluster (cluster 4 in 3.3.2, Fig. 6a) because
777 of the high magnitude of its accumulated mode peak, its timing (April), and the enhanced
778 organic carbon contribution to AOD in the area (Fig. 8b). Though the absolute black carbon
779 contribution to AOD was highest here compared to the other case studies, and in general for the
780 AERONET data, it was organic carbon that was more prevalent in terms of contribution to total
781 AOD. Smoke is comprised of both soot carbon and organic carbon, amongst other constituents
782 (Reid et al., 2005).



783

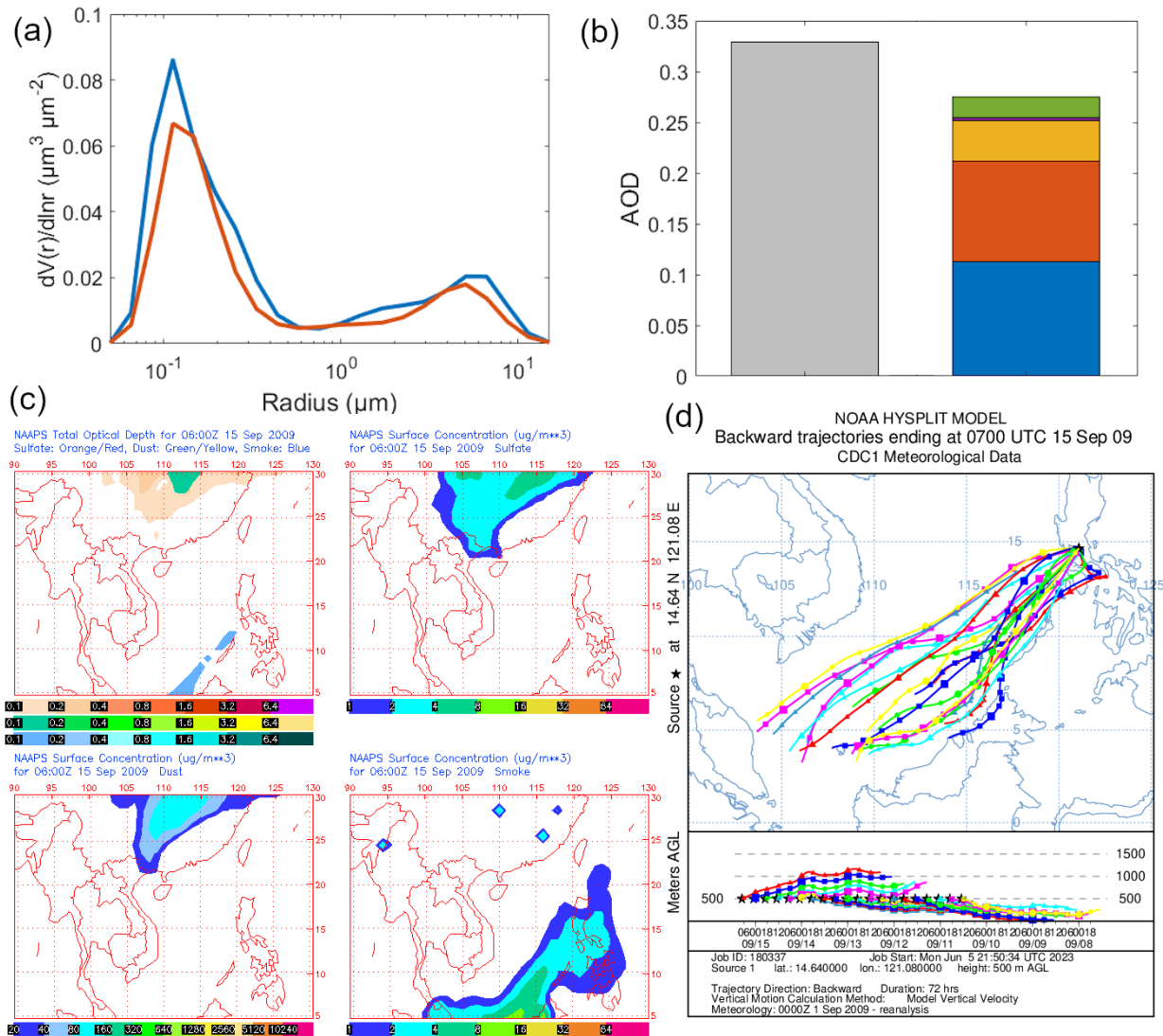
Apr 1 02:30:48 2010 NRL/Monterey Aerosol Modelling

784 **Figure 8:** Case study of long-range transport (smoke – East Asia) around 1 April 2010. (a)
 785 AERONET VSDs at (blue) 00:01 and (red) 00:26 UTC, (b) AOD from AERONET (gray:
 786 median AOD at 500 nm) and MERRA-2 hourly (green: black carbon, violet: dust, yellow: sea
 787 salt, orange: organic carbon, blue: sulfate) compositional contributions to AOD (550 nm) closest
 788 in time to 00:01 UTC, (c) NAAPS maps of total and compositional hourly AOD (orange/red:
 789 sulfate, green/yellow: dust, blue: smoke) and sulfate, dust, and smoke surface concentrations at
 790 00:00 UTC, and (d) HYSPLIT seven-day back-trajectories arriving at Manila Observatory at
 791 00:00 UTC.

792 The smoke contribution to AOD from NAAPS (Fig. 8c) for the first smoke case was visible in
 793 the Philippines (0.2) and seemed to come from East Asia were the smoke contribution to AOD
 794 was greater (reaching 0.8) especially in Peninsular Southeast Asia. Smoke surface concentrations
 795 were also widespread (Fig. 8c) with greatest concentrations in East Asia that reached the
 796 Western Philippines, though seemingly disconnected over the sea. There were observed biomass
 797 burning emissions in the Peninsular Southeast Asia (southern China, Burma, and Thailand) at

798 this time (Shen et al., 2014). The direction of the air mass coming into Metro Manila was from
799 the northeast, which curved from the west in the direction of East Asia based on HYSPLIT back-
800 trajectories (Fig. 8d).

801 The second smoke case was on 15 September 2009 with the source being Southeast Asia. The
802 back-trajectories of this case study (Fig. 9d) are from the southwest of the Philippines, and in the
803 direction of the Malaysia and Indonesia. NAAPS maps likewise show elevated AOD,
804 specifically smoke contribution to AOD (Fig. 9c), as well as enhanced smoke surface
805 contributions in the area around Metro Manila for this second smoke case study. The observed
806 AOD and smoke surface concentration increased specifically from the southwest of the
807 Philippines in the same direction of the back-trajectories. There were fires in the lowland (peat)
808 forests of Borneo around this time (NASA, 2009). MERRA-2 AOD contributions for this case
809 were greatest due to organic carbon as well as sulfate (Fig. 9b), and the absolute black carbon
810 contributions were greatest compared to other cases. The VSD of this smoke case from Southeast
811 Asia (Fig. 9a) resembled that from long-range transported smoke from East Asia (Fig. 8a) and
812 the urban/industrial air mass (cluster 4, Fig. 6a). This case occurred in the afternoon, which was
813 the prevalent time that the urban/industrial air mass was observed (Fig. 6c).

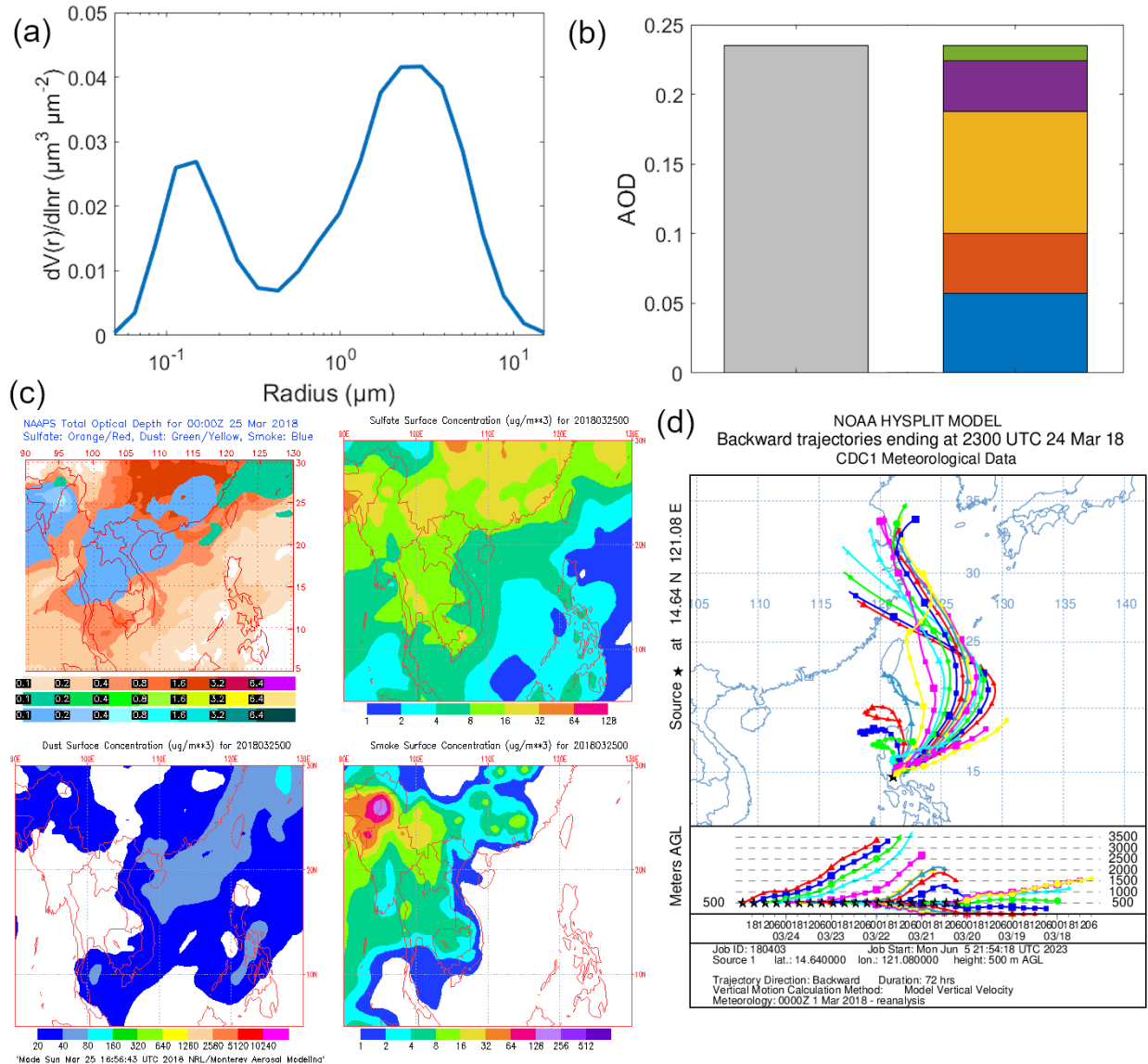


814
 815 **Figure 9:** Case study of long-range transport (smoke – Southeast Asia) around 15 September
 816 2009. (a) AERONET VSDs at (blue) 07:27 and (red) 07:52 UTC, (b) AOD from AERONET
 817 (gray: median AOD at 500 nm) and MERRA-2 hourly (green: black carbon, violet: dust, yellow:
 818 sea salt, orange: organic carbon, blue: sulfate) compositional contributions to AOD (550 nm)
 819 closest in time to 07:27 UTC, (c) NAAPS maps of total and compositional hourly AOD
 820 (orange/red: sulfate, green/yellow: dust, blue: smoke) and sulfate, dust, and smoke surface
 821 concentrations at 06:00 UTC, and (d) HYSPLIT seven-day back-trajectories arriving at Manila
 822 Observatory at 07:00 UTC.
 823

824 3.4.2 Long Range Transport of Dust

825 The VSD of this specific case on 24 March 2018 (Fig. 10a) was most similar to the mixed dust
 826 cluster (cluster 3), which had a mixed size distribution but a more dominant coarse contribution.
 827 This is consistent with the most dominant contribution to AOD in the area, which was sea salt
 828 and dust (Fig. 10b). The back-trajectories were from East Asia around the same latitude as
 829 Taiwan (Fig. 10d). That area, at that time, had increased AOD in general from sulfate and dust

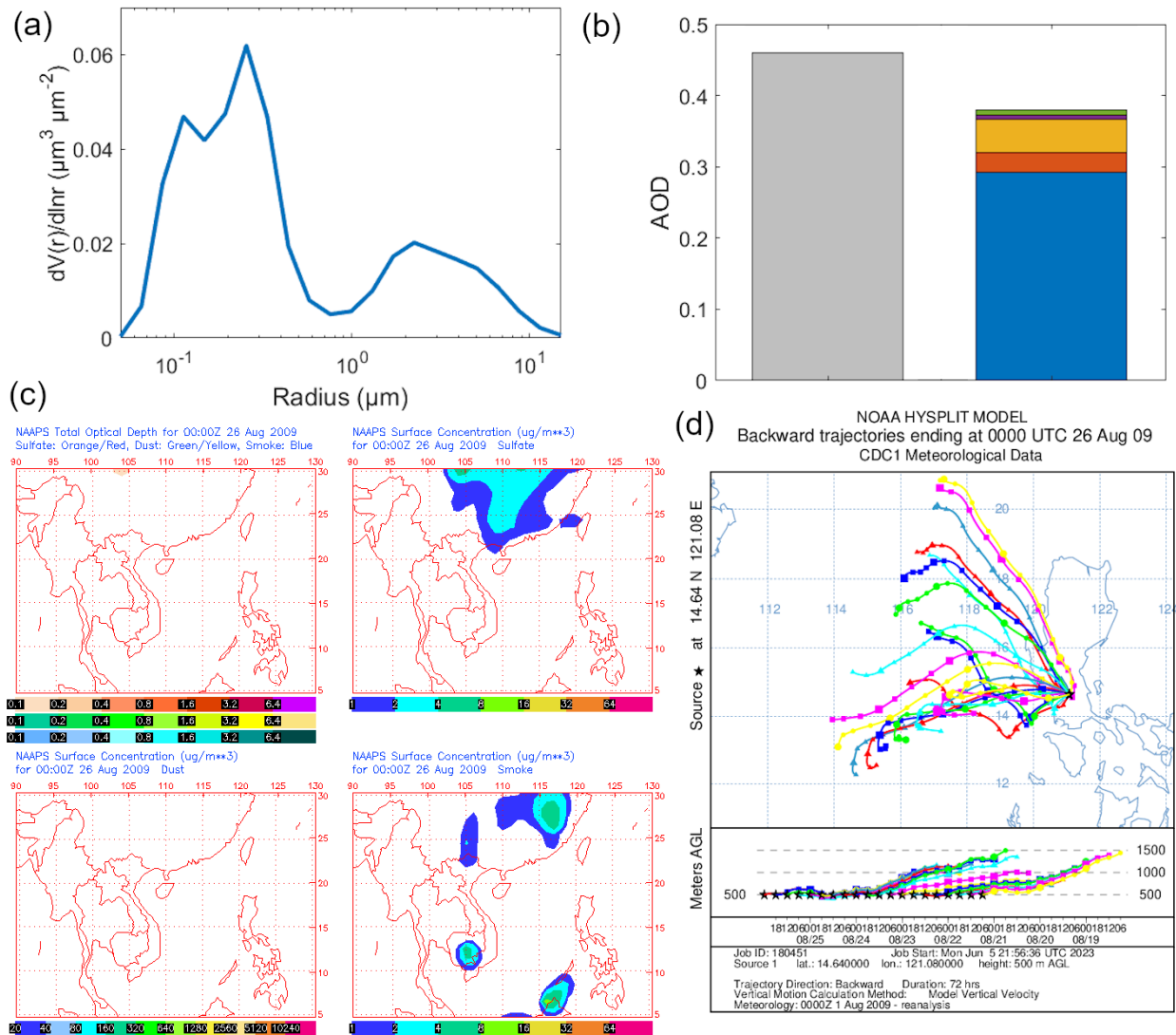
830 (Fig. 10c). The AOD from both AERONET and MERRA-2 (Fig. 10b) are lower than 0.3 (the
 831 AOD threshold for dust in other studies, Table 2) because of the long distance from the source
 832 (thousands of kilometers). The dust and sulfate seemed to have been transported to Metro Manila
 833 from East Asia based on the NAAPS sulfate and dust surface concentrations (Fig. 10c).
 834



835 **Figure 10:** Case study of long-range transport (dust) around 24-25 March 2018. (a) AERONET
 836 VSD at (blue) 23:23 UTC, (b) AOD from AERONET (gray: AOD at 500 nm) and MERRA-2
 837 hourly (green: black carbon, violet: dust, yellow: sea salt, orange: organic carbon, blue: sulfate)
 838 compositional contributions to AOD (550 nm) closest in time to 23:23 UTC, (c) NAAPS maps of
 839 total and compositional hourly AOD (orange/red: sulfate, green/yellow: dust, blue: smoke) and
 840 sulfate, dust, and smoke surface concentrations at 00:00 UTC on March 25, and (d) HYSPLIT
 841 seven-day back-trajectories arriving at Manila Observatory at 23:00 UTC.
 842

843
 844 3.4.3 Cloud Processing

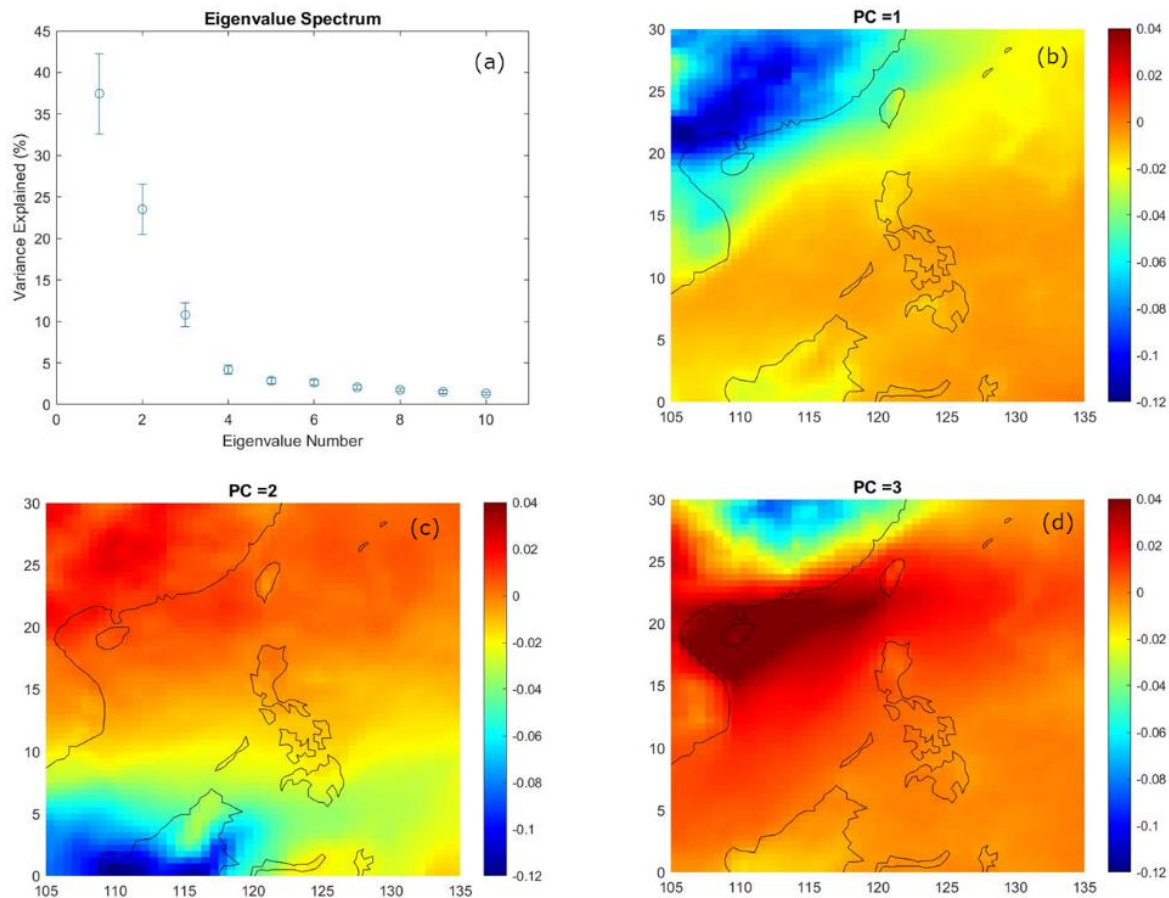
845 Sulfate dominated the AOD (Fig. 11b) for this case on 26 August 2009 in the area around Metro
846 Manila. This along with its VSD exhibiting a second peak (Fig. 11a) in the accumulation mode
847 make it very similar to the cloud processing cluster (cluster 5). Sulfate has been known to be
848 enhanced through chemical productions in clouds and is used as a signature for cloud processing
849 (Barth et al., 2000; Ervens et al., 2018). Aqueous production of sulfate is significant in areas with
850 sources and clouds (Barth et al., 2000), and this case study has both. Aside from the high sulfate
851 contribution to AOD, the cloud fraction (Aqua/MODIS, Terra/MODIS, Fig. S3) is very high
852 (~100%) in the area of the back-trajectories (Fig. 11d). Interestingly, there is no regional AOD
853 elevation observed in the NAAPS maps (Fig. 11c) for this time. There are increased surface
854 smoke and sulfate levels in East Asia as well as southwest of the Philippines, and though the
855 back-trajectories do show a northeastward direction, they do not reach far enough into mainland
856 East Asia. It is possible that even while there are known regional sources of sulfate in Southeast
857 Asia (Smith et al., 2011; Li et al., 2017), this case could be local to the Philippines. There is in
858 fact a large power plant northwest of Metro Manila (Jamora et al., 2020).
859



860
 861 **Figure 11:** Case study of cloud processing on 26 August 2009. (a) AERONET VSDs at 00:18
 862 UTC, (b) AOD from AERONET (gray: median AOD at 500 nm) and MERRA-2 hourly (green:
 863 black carbon, violet: dust, yellow: sea salt, orange: organic carbon, blue: sulfate) compositional
 864 contributions to AOD (550 nm) closest in time to 00:18 UTC, (c) NAAPS maps of total and
 865 compositional hourly AOD and contributions and smoke surface concentrations at 00:00 UTC,
 866 and (d) HYSPLIT seven-day back-trajectories arriving at Manila Observatory at 00:00 UTC.
 867

868 3.5 EOF Analysis of AOD in Southeast Asia

869
 870 The air masses in Metro Manila are influenced by regional sources which were identified
 871 through EOF analysis of AOD. Three principal components (PC, Fig. 12) explained most of the
 872 data variance (73.77%) (Fig. 12a) and were all well-separated from each other and are therefore
 873 most probably the major distinct aerosol particle sources in the region. They will be the focus of
 874 the subsequent discussion.



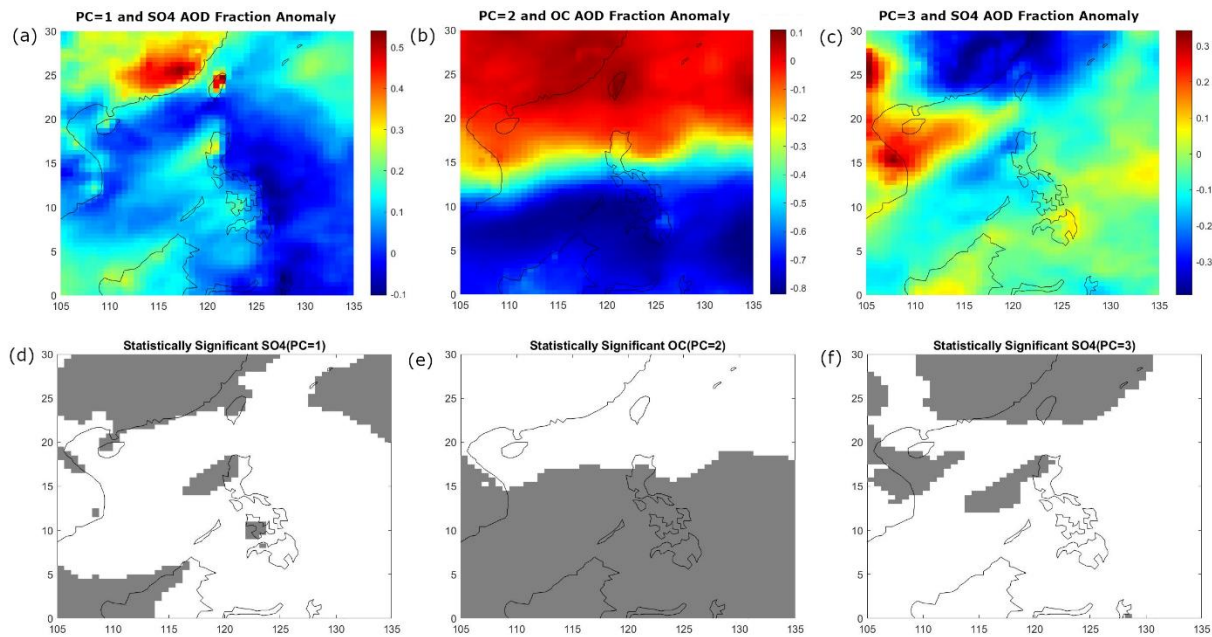
875
 876 **Figure 12:** Results of the singular value decomposition. (a) Eigenvalue spectrum of the first ten
 877 eigenvalues, (b-d) maps of the coefficients of regression AOD anomalies onto the first three
 878 principal components.

879 The first PC explains 37.46% of the data variance (Fig. 12a) and, based on the map of the
 880 regression coefficients (Fig. 12b), separates mainland East Asia from the Philippines and
 881 Indonesia. East Asia is a globally recognized source for high AOD (Li et al., 2013), and its
 882 contribution to particles in Southeast Asia possibly corresponds to the first PC. The second PC
 883 explains 25.51% of the data variance (Fig. 12a) and separates southern Southeast Asia from
 884 northern Southeast Asia at around 15°N (Fig. 12c). Southern Southeast Asia is a known regional
 885 source of aerosol particles due to biomass burning (Cohen et al., 2017) and could be associated
 886 with the second PC. The third PC explains 10.80% of the data variance (Fig. 12a) and separates
 887 northern East Asia from southern East Asia mainland and the rest of Southeast Asia (Fig. 12d).

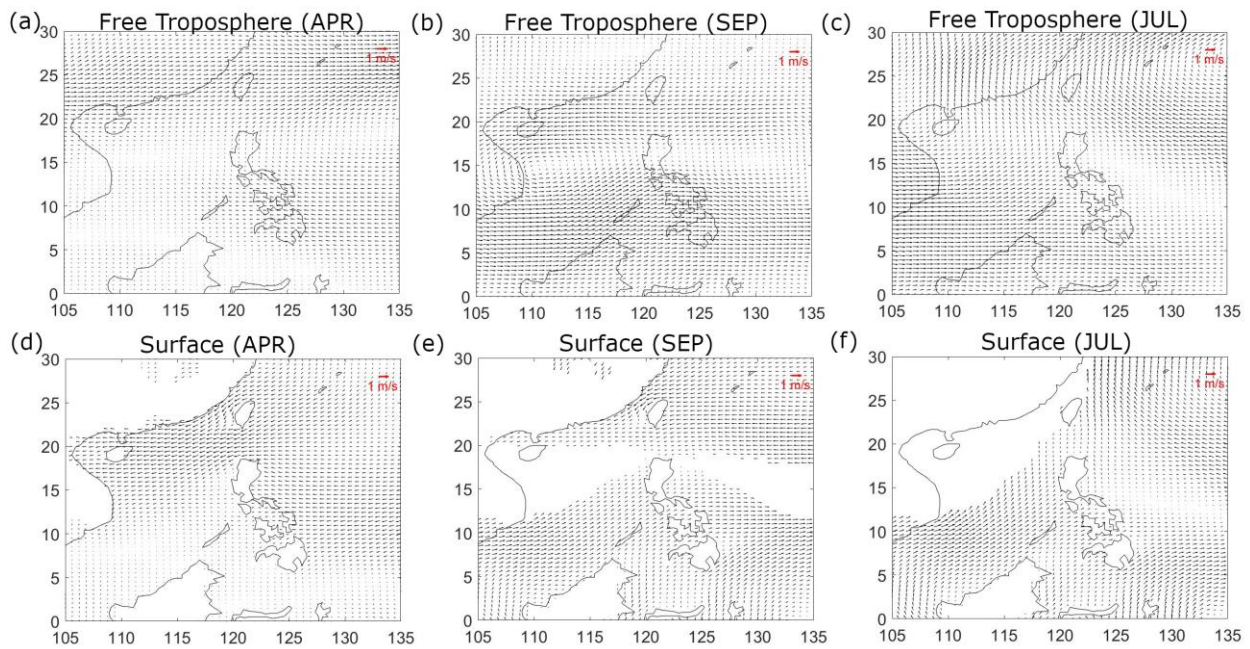
888 To gain confidence in the association of the PCs with their sources, we present correlation maps
 889 between the first three PCs to the fractional contributions of sulfate and organic carbon to AOD
 890 for the entire dataset.

891 The correlation maps of the first PC and the sulfate contribution to AOD (Fig. 13a and 13d)
 892 show high and statistically significant correlations (gray areas) in mainland East Asia and
 893 Taiwan, parts of western Philippines and Borneo, which are the probable sulfate sources. Clues
 894 from the mean monthly wind vector maps in April (Fig. 14a and 14d) and mean monthly AOD in

895 either March or April (Fig. S3c or S3e) most resembling the features of regression map of the
 896 first PC (Fig. 12b) and the PC time series peaking in March (Fig. S4) together suggest that the
 897 first PC may be associated with air masses that are present around March or April. Emissions
 898 sources and meteorology that are dominant during the peak dates in the PC time series offer
 899 clues to the attribution of each PC. The Southeast Asia region and the Philippines is influenced
 900 by the monsoon systems (Coronas, 1920; Matsumoto et al., 2020) and February to March is the
 901 time when the winds are transitioning from the northeasterly to easterly. The first PC could be
 902 affected by the easterly winds, which are dominant around March when its PC values peaked.
 903 The higher-level winds (free troposphere) (Fig. 14a) in April are from the west in mainland East
 904 Asia and are from the east in the Philippines and it is possible that the different wind regimes are
 905 distinguishing the sulfate sources in East Asia and the Philippines and beyond. Sulfate is a
 906 known product of industry in East Asia (Smith et al., 2011; Li et al., 2017) while the West Luzon
 907 and West Visayas islands have large power plants (Jamora et al., 2020).



908 **Figure 13:** Correlation coefficients of principal components with (a/c) sulfate AOD fraction and
 909 (b) organic carbon AOD fraction. Statistically significant (90%, d-f) areas are shaded gray.
 910



911 **Figure 14:** Monthly averaged winds for (a & d) April, (b & e) September, and (c & f) July from
 912 MERRA-2 at (725 hPa, a-c) the free troposphere approximate and at (1000 hPa, d-f) the surface.
 913

914 The correlation maps of the second PC and the OC contribution to AOD (Fig. 13b and 13e) show
 915 high and statistically significant correlations from 0°N to 15°N. The large magnitude of the
 916 correlation coefficient (gray areas in Fig. 13b) stands out in southern Southeast Asia and is the
 917 potential OC source. In this case, it is known that Indonesia is a major source of biomass burning
 918 during its fire season (Glover and Jessup, 1998), and thus the local significance established in the
 919 southern Southeast Asia is most likely due to the Indonesia biomass burning source. The burning
 920 season in Indonesia is from August to October, and that is the same time when the AOD values
 921 peak in the area (Fig. S3h, S3i, and S3j), as well as the peak of the second PC in the time series
 922 (Fig. S4). Winds are usually from the southwest and west due to the southwest monsoon from
 923 September to October, when the second PC peaked, and thus the second PC may be related to the
 924 southwest monsoon. During the same time the surface and free troposphere mean monthly winds
 925 (Fig. 14b and 14e) are from the southwest (in the general direction of Indonesia) towards the
 926 south portion of Southeast Asia and thus corroborate the observation that the second PC may be
 927 highlighting the regional effect of the Indonesia forest fires. Of interest is the line of separation
 928 of the northern and southern Southeast Asia in the principal component that is within the area of
 929 the monsoon trough (Wang et al., 2007). This line is also evident in the surface and the free
 930 troposphere maps where the southwest winds from the area of Indonesia meet the easterlies in
 931 north Southeast Asia (Fig. 14b and 14e) and which thus appears to be limiting the dispersion of
 932 the biomass burning emissions to southern Southeast Asia.

933 The third PC was also well correlated to the sulfate AOD fraction though, compared to the first
 934 PC correlation maps, there were distinctions between the northern and southern East Asia
 935 regions (Fig. 13c and 13f). The local Philippine source still came out in the correlation maps as a
 936 significant source. It was not clear from the PC time series (Fig. S4), which showed peaks in the
 937 third PC in February, how the dates were related to the PC profile. The free troposphere winds in
 938 July (Fig. 14c), as well as the AOD monthly mean map in July (Fig. 14c), however, showed

939 more similarities to the third PC regression map. Both showed a delineation between the
940 northern East Asia and southern East Asia (including Hong Kong) features. Mean winds (Fig.
941 14c) in the free troposphere are from the west, due to the southwest monsoon, in the area around
942 the Philippines, and they were from the northeast in north Southeast Asia. The interface of the
943 winds is within the approximate location of the monsoon trough in July (Wang et al., 2007), and
944 it is thus possible that the monsoon trough is causing the separation of the sulfate sources. This
945 could be investigated further. The monsoon trough has been noted to scavenge aerosol particles
946 from southern Southeast Asia (Reid et al., 2013). It is evident from the analysis that meteorology
947 affects the transport and processing of aerosol particles in region which along with local sources
948 contribute to the aerosol composition in Southeast Asia (Cruz et al., 2019; AzadiAghdam et al.,
949 2019; Braun et al., 2020; Hilario et al., 2020b; Hilario et al., 2022).

950

951 **4. Conclusion**

952 Metro Manila has both urban and industrial local sources known to contribute to the dominance
953 of fine mode particles in its air (Cruz et al., 2019). Ten years of AERONET data in Manila
954 Observatory suggest that aerosol particles in Metro Manila were mixed in size but with a
955 prevalent fine mode fraction (>50% FMF) throughout the year. Background clean marine aerosol
956 particles (58% of the time) and fine polluted aerosol particles (20% of the time) were the most
957 dominant clear sky day sources impacting the atmospheric column over Metro Manila based on
958 cluster analysis of volume size distributions. The proximity of Metro Manila to the sea, both in
959 the east and west, along with local sources, transportation being the most prominent, together
960 contribute to the prevalence of the marine and fine particles. The prevalence of marine particles
961 could explain the relatively small AOD values in Metro Manila compared to other Southeast
962 Asian megacities (Reid et al., 2013).

963 Regional sources and meteorology also impact monthly aerosol optical depth trends in Metro
964 Manila from EOF analysis. Biomass burning from Borneo and Sumatra emerged in the study as
965 the second most prevalent regional anthropogenic aerosol particle source in Southeast Asia.
966 Though the monsoon trough limits the dispersion of aerosol particles throughout the entire
967 Southeast Asia, biomass burning emissions impact southern Southeast Asia including Metro
968 Manila during the southwest monsoon (July to September). The monsoon winds facilitate the
969 transport of fine particles during the peak burning season in Borneo and Sumatra (August-
970 September). This is experienced in Metro Manila as higher than usual aerosol particle loadings
971 around the same period (August to October). Climatologically, August was also when there were
972 particles with the greatest fine mode fractions that were relatively absorbing and non-
973 hygroscopic possibly due to increased organic and elemental carbon fractional contributions.
974 Though not as strong a source as the Borneo and Sumatra case, the peninsular Southeast Asia
975 burning season (March-April) also contributed to extreme aerosol particle concentrations over
976 Metro Manila.

977 High aerosol particle loadings due to transported dust, probably from East Asia, were observed
978 in Metro Manila during the transition period between the southwest and northeast monsoons and
979 during the northeast monsoon (December to February). These extreme events are transient
980 because the lowest median aerosol particle loadings of the year were observed during the
981 northeast monsoon when annual wind speeds were highest. Particles then were observed to be
982 largest in diameter, with the greatest coarse fraction contribution, relatively high absorptivity,

983 and most hygroscopicity, compared to other months of the year. This is probably due to
984 constituents other than soot, especially aged dust (Kim and Park, 2012; Geng et al., 2014) and
985 sea salt which the northeast winds appear to be bringing in from the general direction of the
986 Luzon Island and the Philippine Sea (West Pacific Ocean).

987 Cloud processing is one of the cases that were linked to very high aerosol particle loading in
988 Metro Manila. This is associated with sulfate sources, which appear more localized in nature
989 because of a power plant nearby. This sulfate source seems to be distinct from the industrial
990 sulfate air mass from East Asia, which is the most dominant regional aerosol particle source in
991 Southeast Asia (Li et al., 2013). Winds appear to limit the mixing of this notable East Asia air
992 mass with local industrial sources in the region including the Philippines and Indonesia.

993 The formation of cloud systems in Southeast Asia is complex due to intersecting large- and
994 small-scale mechanisms. Additionally, the interaction of particles and clouds in Southeast Asia is
995 not yet well understood. In Metro Manila, both topography and meteorology affect aerosol
996 particle distribution (Cruz et al., 2023). This baseline study on the aerosol particle characteristics
997 in Metro Manila and in regional Southeast Asia shows how meteorology impacts varied aerosol
998 particle sources (e.g., sulfate, elemental carbon, and organic carbon) and their distribution in the
999 region. This can help in mitigating aerosol particle sources in the region and in the deepening of
1000 the understanding of the relationship of aerosol particles, meteorology, and clouds.

1001

1002 **Data availability**

1003 Aerosol Robotic Network (AERONET) (2020), Version 3 Direct Sun Algorithm, Site: Manila
1004 Observatory, Philippines, Accessed: [**28 September 2020**], [https://aeronet.gsfc.nasa.gov/cgi-](https://aeronet.gsfc.nasa.gov/cgi-bin/webtool_aod_v3?stage=3®ion=Asia&state=Philippines&site=Manila_Observatory&place_code=10&if_polarized=0)
1005 [bin/webtool_aod_v3?stage=3®ion=Asia&state=Philippines&site=Manila_Observatory&plac](https://aeronet.gsfc.nasa.gov/cgi-bin/webtool_aod_v3?stage=3®ion=Asia&state=Philippines&site=Manila_Observatory&place_code=10&if_polarized=0)
1006 [e_code=10&if_polarized=0](https://aeronet.gsfc.nasa.gov/cgi-bin/webtool_aod_v3?stage=3®ion=Asia&state=Philippines&site=Manila_Observatory&place_code=10&if_polarized=0)

1007 Aerosol Robotic Network (AERONET) (2020), Version 3 Direct Sun and Inversion Algorithm,
1008 Site: Manila Observatory, Philippines, Accessed: [**28 September 2020**],
1009 [https://aeronet.gsfc.nasa.gov/cgi-](https://aeronet.gsfc.nasa.gov/cgi-bin/webtool_inv_v3?stage=3®ion=Asia&state=Philippines&site=Manila_Observatory&place_code=10&if_polarized=0)
1010 [bin/webtool_inv_v3?stage=3®ion=Asia&state=Philippines&site=Manila_Observatory&place](https://aeronet.gsfc.nasa.gov/cgi-bin/webtool_inv_v3?stage=3®ion=Asia&state=Philippines&site=Manila_Observatory&place_code=10&if_polarized=0)
1011 [_code=10&if_polarized=0](https://aeronet.gsfc.nasa.gov/cgi-bin/webtool_inv_v3?stage=3®ion=Asia&state=Philippines&site=Manila_Observatory&place_code=10&if_polarized=0)

1012 Multi-angle Imaging SpectroRadiometer (MISR) Jet Propulsion Laboratory (2018), Level 3
1013 Component Global Aerosol product in netCDF format covering a month V004, Accessed: [**22**
1014 **November 2021**], <https://search.earthdata.nasa.gov/>

1015 Global Modeling and Assimilation Office (GMAO) (2015), MERRA-2 inst3_3d_asm_Np: 3d,3-
1016 Hourly,Instantaneous,Pressure-Level,Assimilation,Assimilated Meteorological Fields V5.12.4,
1017 Greenbelt, MD, USA, Goddard Earth Sciences Data and Information Services Center (GES
1018 DISC), Accessed: [**10 March 2021**], <https://doi.org/10.5067/QBZ6MG944HW0>

1019 Global Modeling and Assimilation Office (GMAO) (2015), MERRA-2 tavg1_2d_flux_Nx: 2d,1-
1020 Hourly,Time-Averaged,Single-Level,Assimilation,Surface Flux Diagnostics V5.12.4, Greenbelt,
1021 MD, USA, Goddard Earth Sciences Data and Information Services Center (GES DISC),
1022 Accessed: [**10 March 2021**], <https://doi.org/10.5067/7MCPBJ41Y0K6>

1023 Global Modeling and Assimilation Office (GMAO) (2015), MERRA-2 tavg1_2d_csp_Nx: 2d,1-
1024 Hourly,Time-averaged,Single-Level,Assimilation,COSP Satellite Simulator V5.12.4, Greenbelt,
1025 MD, USA, Goddard Earth Sciences Data and Information Services Center (GES DISC),
1026 Accessed: [**13 July 2021**], <https://doi.org/10.5067/H0VVAD8F6MX5>

1027 Nguyen, P., E.J. Shearer, H. Tran, M. Ombadi, N. Hayatbini, T. Palacios, P. Huynh, G.
1028 Updegraff, K. Hsu, B. Kuligowski, W.S. Logan, and S. Sorooshian, The CHRS Data Portal, an
1029 easily accessible public repository for PERSIANN global satellite precipitation data, Nature
1030 Scientific Data, Vol. 6, Article 180296, 2019, Accessed: [**11 March 2021**],
1031 <https://doi.org/10.1038/sdata.2018.296>

1032

1033 **Author contributions**

1034 GRL and AS designed the experiment. NL, SNU, GRL, GFG, HJO, JBS, and MTC, carried out
1035 various aspects of the data collection. GRL, AS, JBS, MOC, MRH, CC, and LDG conducted
1036 analysis and interpretation of the data. GRL prepared the manuscript draft with contributions
1037 from the coauthors. AFA, LDG, MRH, GRL, and AS reviewed and edited the manuscript. AS
1038 led the management and funding acquisition. All authors approved the final version of the
1039 manuscript.

1040

1041 **Competing interests**

1042 We declare that Armin Sorooshian is a member of the editorial board of Atmospheric Chemistry
1043 and Physics. The peer-review process was guided by an independent editor, and the authors have
1044 also no other competing interests to declare.

1045

1046 **Acknowledgements**

1047 The authors acknowledge support from NASA grant 80NSSC18K0148 in support of the NASA
1048 CAMP²Ex project, in addition to ONR grant N00014-21-1-2115. We acknowledge the US Naval
1049 Research Laboratory for providing the AERONET instrument. We acknowledge the use of
1050 imagery from the NASA Worldview application (<https://worldview.earthdata.nasa.gov>), part of
1051 the NASA Earth Observing System Data and Information System (EOSDIS).

1052

1053 **References:**

1054 AERONET Inversion Products (Version 3):

1055 https://aeronet.gsfc.nasa.gov/new_web/Documents/Inversion_products_for_V3.pdf, access: June
1056 25, 2021, 2019.

1057 Alas, H. D., Müller, T., Birmili, W., Kecorius, S., Cambaliza, M. O., Simpas, J. B. B., Cayetano,
1058 M., Weinhold, K., Vallar, E., and Galvez, M. C.: Spatial characterization of black carbon mass
1059 concentration in the atmosphere of a southeast asian megacity: an air quality case study for
1060 Metro Manila, Philippines, Aerosol Air Qual. Res., 18, 2301-2317,
1061 <https://doi.org/10.4209/aaqr.2017.08.0281>, 2018.

- 1062 Aldhaif, A. M., Lopez, D. H., Dadashazar, H., and Sorooshian, A.: Sources, frequency, and
 1063 chemical nature of dust events impacting the United States East Coast, *Atmos. Environ.*, 231,
 1064 117456, <https://doi.org/10.1016/j.atmosenv.2020.117456>, 2020.
- 1065 Aldhaif, A. M., Lopez, D. H., Dadashazar, H., Painemal, D., Peters, A. J., and Sorooshian, A.:
 1066 An Aerosol Climatology and Implications for Clouds at a Remote Marine Site: Case Study Over
 1067 Bermuda, *J. Geophys. Res.- Atmos.*, 126, e2020JD034038,
 1068 <https://doi.org/10.1029/2020JD034038>, 2021.
- 1069 Alizadeh-Choozari, O., and Gharaylou, M.: Aerosol impacts on radiative and microphysical
 1070 properties of clouds and precipitation formation, *Atmos. Res.*, 185, 53-64,
 1071 <https://doi.org/10.1016/j.atmosres.2016.10.021>, 2017.
- 1072 Amnuaylojaroen, T.: Air Pollution Modeling in Southeast Asia—An Overview, *Vegetation Fires
 1073 and Pollution in Asia*, 531-544, https://doi.org/10.1007/978-3-031-29916-2_31, 2023.
- 1074 Ångström, A.: On the atmospheric transmission of sun radiation and on dust in the air,
 1075 *Geografiska Annaler*, 11, 156-166, 1929.
- 1076 Arthur, D., and Vassilvitskii, S.: *k-means++: The advantages of careful seeding*, Stanford, 2006.
- 1077 AzadiAghdam, M., Braun, R. A., Edwards, E.-L., Bañaga, P. A., Cruz, M. T., Betito, G.,
 1078 Cambaliza, M. O., Dadashazar, H., Lorenzo, G. R., and Ma, L.: On the nature of sea salt aerosol
 1079 at a coastal megacity: Insights from Manila, Philippines in Southeast Asia, *Atmos. Environ.*, 216,
 1080 116922, <https://doi.org/10.1016/j.atmosenv.2019.116922>, 2019.
- 1081 Bagtasa, G.: Contribution of tropical cyclones to rainfall in the Philippines, *Journal of Climate*,
 1082 30, 3621-3633, 2017.
- 1083 Bañares, E. N., Narisma, G. T. T., Simpas, J. B. B., Cruz, F. A. T., Lorenzo, G. R. H.,
 1084 Cambaliza, M. O. L., and Coronel, R. C.: Seasonal and diurnal variations of observed convective
 1085 rain events in metro Manila, Philippines, *Atmos. Res.*, 105646,
 1086 <https://doi.org/10.1016/j.atmosres.2021.105646>, 2021.
- 1087 Barth, M., Rasch, P., Kiehl, J., Benkovitz, C., and Schwartz, S.: Sulfur chemistry in the National
 1088 Center for Atmospheric Research Community Climate Model: Description, evaluation, features,
 1089 and sensitivity to aqueous chemistry, *J. Geophys. Res.- Atmos.*, 105, 1387-1415,
 1090 <https://doi.org/10.1029/1999JD900773>, 2000.
- 1091 Bautista VII, A. T., Pabroa, P. C. B., Santos, F. L., Racho, J. M. D., and Quirit, L. L.:
 1092 Carbonaceous particulate matter characterization in an urban and a rural site in the Philippines,
 1093 *Atmospheric Pollution Research*, 5, 245-252, <https://doi.org/10.5094/APR.2014.030>, 2014.
- 1094 Bergstrom, R. W., Russell, P. B., and Hignett, P.: Wavelength dependence of the absorption of
 1095 black carbon particles: Predictions and results from the TARFOX experiment and implications
 1096 for the aerosol single scattering albedo, *J. Atmos. Sci.*, 59, 567-577,
 1097 [https://doi.org/10.1175/1520-0469\(2002\)059<0567:WDOTAO>2.0.CO;2](https://doi.org/10.1175/1520-0469(2002)059<0567:WDOTAO>2.0.CO;2), 2002.

- 1098 Bergstrom, R. W., Pilewskie, P., Schmid, B., and Russell, P. B.: Estimates of the spectral aerosol
 1099 single scattering albedo and aerosol radiative effects during SAFARI 2000, *J. Geophys. Res.-*
 1100 *Atmos.*, 108, <https://doi.org/10.1029/2002JD002435>, 2003.
- 1101 Bergstrom, R. W., Pilewskie, P., Russell, P. B., Redemann, J., Bond, T. C., Quinn, P. K., and
 1102 Sierau, B.: Spectral absorption properties of atmospheric aerosols, *Atmos. Chem. Phys.*, 7, 5937-
 1103 5943, <https://doi.org/10.5194/acp-7-5937-2007>, 2007.
- 1104 Bi, J., Huang, J., Hu, Z., Holben, B., and Guo, Z.: Investigating the aerosol optical and radiative
 1105 characteristics of heavy haze episodes in Beijing during January of 2013, *J. Geophys. Res.-*
 1106 *Atmos.*, 119, 9884-9900, <https://doi.org/10.1002/2014JD021757>, 2014.
- 1107 Björnsson, H., and Venegas, S.: A manual for EOF and SVD analyses of climatic data, CCGCR
 1108 Report, 97, 112-134, 1997.
- 1109 Bohren, C. F., and Clothiaux, E. E.: Fundamentals of atmospheric radiation: an introduction with
 1110 400 problems, John Wiley & Sons, 2006.
- 1111 Braun, R. A., Aghdam, M. A., Bañaga, P. A., Betito, G., Cambaliza, M. O., Cruz, M. T.,
 1112 Lorenzo, G. R., MacDonald, A. B., Simpas, J. B., and Stahl, C.: Long-range aerosol transport
 1113 and impacts on size-resolved aerosol composition in Metro Manila, Philippines, *Atmos. Chem.*
 1114 *Phys.*, 20, 2387-2405, <https://doi.org/10.5194/acp-20-2387-2020>, 2020.
- 1115 Buchard, V., Randles, C., Da Silva, A., Darmenov, A., Colarco, P., Govindaraju, R., Ferrare, R.,
 1116 Hair, J., Beyersdorf, A., and Ziemba, L.: The MERRA-2 aerosol reanalysis, 1980 onward. Part
 1117 II: Evaluation and case studies, *Journal of Climate*, 30, 6851-6872, <https://doi.org/10.1175/JCLI->
 1118 [D-16-0613.1](https://doi.org/10.1175/JCLI-D-16-0613.1), 2017.
- 1119 Cahyono, W. E., Setyawati, W., Hamdi, S., Cholianawati, N., Kombara, P. Y., and Sari, W. J.:
 1120 Observations of aerosol optical properties during tropical forest fires in Indonesia, *Materials*
 1121 *Today: Proceedings*, 63, S445-S450, <https://doi.org/10.1016/j.matpr.2022.04.113>, 2022.
- 1122 Caido, N. G., Ong, P. M., Rempillo, O., Galvez, M. C., and Vallar, E.: Spatiotemporal analysis
 1123 of MODIS aerosol optical depth data in the Philippines from 2010 to 2020, *Atmosphere*, 13, 939,
 1124 <https://doi.org/10.3390/atmos13060939>, 2022.
- 1125 Chang, C.-P., Wang, Z., McBride, J., and Liu, C.-H.: Annual cycle of Southeast Asia—Maritime
 1126 Continent rainfall and the asymmetric monsoon transition, *Journal of climate*, 18, 287-301,
 1127 <https://doi.org/10.1175/JCLI-3257.1>, 2005.
- 1128 Che, H., Xia, X., Zhu, J., Wang, H., Wang, Y., Sun, J., Zhang, X., and Shi, G.: Aerosol optical
 1129 properties under the condition of heavy haze over an urban site of Beijing, China, *Environ. Sci.*
 1130 *Pollut. R.*, 22, 1043-1053, <https://doi.org/10.1007/s11356-014-3415-5>, 2015.
- 1131 Chen, Q., McGowan, S., Gouramanis, C., Fong, L., Balasubramanian, R., and Taylor, D.:
 1132 Rapidly rising transboundary atmospheric pollution from industrial and urban sources in
 1133 Southeast Asia and its implications for regional sustainable development, *Environ. Res. Lett.*, 15,
 1134 1040a1045, <https://doi.org/10.1088/1748-9326/abb5ce>, 2020.

1135 Choi, M., Lim, H., Kim, J., Lee, S., Eck, T. F., Holben, B. N., Garay, M. J., Hyer, E. J., Saide, P.
1136 E., and Liu, H.: Validation, comparison, and integration of GOCI, AHI, MODIS, MISR, and
1137 VIIRS aerosol optical depth over East Asia during the 2016 KORUS-AQ campaign, *Atmos.*
1138 *Meas. Tech.*, 12, 4619-4641, <https://doi.org/10.5194/amt-12-4619-2019>, 2019.

1139 Cohen, J. B.: Quantifying the occurrence and magnitude of the Southeast Asian fire climatology,
1140 *Environmental Research Letters*, 9, 114018, <https://dx.doi.org/10.1088/1748-9326/9/11/114018>,
1141 2014.

1142 Cohen, J. B., Lecoœur, E., and Hui Loong Ng, D.: Decadal-scale relationship between
1143 measurements of aerosols, land-use change, and fire over Southeast Asia, *Atmos. Chem. Phys.*,
1144 17, 721-743, <https://doi.org/10.5194/acp-17-721-2017>, 2017.

1145 Coronas, J.: *The Climate and Weather of the Philippines, 1903-1918*, by Rev. José Coronas. SJ,
1146 Chief, Meteorological Division, Weather Bureau, Manila Observatory, Manila.: Bureau of
1147 Printing, 1920.

1148 Crosbie, E., Sorooshian, A., Monfared, N. A., Shingler, T., and Esmaili, O.: A multi-year aerosol
1149 characterization for the greater Tehran area using satellite, surface, and modeling data,
1150 *Atmosphere*, 5, 178-197, <https://doi.org/10.3390/atmos5020178>, 2014.

1151 Crosbie, E., Ziemba, L. D., Shook, M. A., Robinson, C. E., Winstead, E. L., Thornhill, K. L.,
1152 Braun, R. A., MacDonald, A. B., Stahl, C., and Sorooshian, A.: Measurement report: Closure
1153 analysis of aerosol–cloud composition in tropical maritime warm convection, *Atmos. Chem.*
1154 *Phys.*, 22, 13269-13302, <https://doi.org/10.5194/acp-22-13269-2022>, 2022.

1155 Cruz, F., Narisma, G. T., Villafuerte II, M. Q., Chua, K. C., and Olaguera, L. M.: A
1156 climatological analysis of the southwest monsoon rainfall in the Philippines, *Atmos. Res.*, 122,
1157 609-616, <https://doi.org/10.1016/j.atmosres.2012.06.010>, 2013.

1158 Cruz, M. T., Bañaga, P. A., Betito, G., Braun, R. A., Stahl, C., Aghdam, M. A., Cambaliza, M.
1159 O., Dadashazar, H., Hilario, M. R., Lorenzo, G. R., Ma, L., MacDonald, A. B., Pabroa, C., Yee,
1160 J. R., Simpas, J. B., and Sorooshian, A.: Size-resolved composition and morphology of
1161 particulate matter during the southwest monsoon in Metro Manila, Philippines, *Atmos. Chem.*
1162 *Phys.*, 19, 10675–10696, <https://doi.org/10.5194/acp-19-10675-2019>, 2019.

1163 Cruz, M. T., Simpas, J. B., Sorooshian, A., Betito, G., Cambaliza, M. O. L., Collado, J. T.,
1164 Eloranta, E. W., Holz, R., Topacio, X. G. V., and Del Socorro, J.: Impacts of regional wind
1165 circulations on aerosol pollution and planetary boundary layer structure in Metro Manila,
1166 Philippines, *Atmos. Environ.*, 293, 119455, <https://doi.org/10.1016/j.atmosenv.2022.119455>,
1167 2023.

1168 Deep, A., Pandey, C. P., Nandan, H., Singh, N., Yadav, G., Joshi, P., Purohit, K., and Bhatt, S.:
1169 Aerosols optical depth and Ångström exponent over different regions in Garhwal Himalaya,
1170 India, *Environmental Monitoring and Assessment*, 193, 324, [https://doi.org/10.1007/s10661-021-](https://doi.org/10.1007/s10661-021-09048-4)
1171 09048-4, 2021.

1172 Di Girolamo, L., Holz, R., Reid, J., Tanelli, S., van den Heever, S., Narsma, G., and Simpas, J.:
1173 Cloud and aerosol monsoonal processes-Philippines experiment (CAMP2Ex), NASA White
1174 Paper, 2015.

1175 Diner, D. J., Di Girolamo, L., and Nolin, A.: Preface to the MISR special issue, *Remote Sens.*
1176 *Environ.*, 107, 1, <https://doi.org/10.1016/j.rse.2006.11.001>, 2007.

1177 Dong, X., and Fu, J. S.: Understanding interannual variations of biomass burning from
1178 Peninsular Southeast Asia, part II: Variability and different influences in lower and higher
1179 atmosphere levels, *Atmospheric Environment*, 115, 9-18,
1180 <https://doi.org/10.1016/j.atmosenv.2015.05.052>, 2015.

1181 Dorado, S. V., Holdsworth, J. L., Lagrosas, N. C., Villarin, J. R., Narisma, G., Ellis, J., and
1182 Perez, R.: Characterization of urban atmosphere of Manila with lidar, filter sampling, and
1183 radiosonde, *Lidar Remote Sensing for Industry and Environment Monitoring*, 2001, 591-598,

1184 Dubovik, O., Holben, B., Kaufman, Y., Yamasoe, M., Smirnov, A., Tanré, D., and Slutsker, I.:
1185 Single-scattering albedo of smoke retrieved from the sky radiance and solar transmittance
1186 measured from ground, *J. Geophys. Res.- Atmos.*, 103, 31903-31923,
1187 <https://doi.org/10.1029/98JD02276>, 1998.

1188 Dubovik, O., and King, M. D.: A flexible inversion algorithm for retrieval of aerosol optical
1189 properties from Sun and sky radiance measurements, *J. Geophys. Res.- Atmos.*, 105, 20673-
1190 20696, <https://doi.org/10.1029/2000JD900282>, 2000.

1191 Dubovik, O., Holben, B., Eck, T. F., Smirnov, A., Kaufman, Y. J., King, M. D., Tanré, D., and
1192 Slutsker, I.: Variability of absorption and optical properties of key aerosol types observed in
1193 worldwide locations, *J. Atmos. Sci.*, 59, 590-608, [https://doi.org/10.1175/1520-0469\(2002\)059<0590:VOAAOP>2.0.CO;2](https://doi.org/10.1175/1520-0469(2002)059<0590:VOAAOP>2.0.CO;2), 2002.

1195 Eck, T., Holben, B., Reid, J., O'Neill, N., Schafer, J., Dubovik, O., Smirnov, A., Yamasoe, M.,
1196 and Artaxo, P.: High aerosol optical depth biomass burning events: A comparison of optical
1197 properties for different source regions, *Geophys. Res. Lett.*, 30,
1198 <https://doi.org/10.1029/2003GL017861>, 2003.

1199 Eck, T., Holben, B., Dubovik, O., Smirnov, A., Goloub, P., Chen, H., Chatenet, B., Gomes, L.,
1200 Zhang, X. Y., and Tsay, S. C.: Columnar aerosol optical properties at AERONET sites in central
1201 eastern Asia and aerosol transport to the tropical mid-Pacific, *J. Geophys. Res.- Atmos.*, 110,
1202 <https://doi.org/10.1029/2004JD005274>, 2005.

1203 Eck, T., Holben, B., Reid, J., Mukelabai, M., Piketh, S., Torres, O., Jethva, H., Hyer, E., Ward,
1204 D., and Dubovik, O.: A seasonal trend of single scattering albedo in southern African
1205 biomass-burning particles: Implications for satellite products and estimates of emissions for the
1206 world's largest biomass-burning source, *J. Geophys. Res.- Atmos.*, 118, 6414-6432,
1207 <https://doi.org/10.1002/jgrd.50500>, 2013.

1208 Eck, T. F., Holben, B., Reid, J., Dubovik, O., Smirnov, A., O'Neill, N., Slutsker, I., and Kinne, S.:
1209 Wavelength dependence of the optical depth of biomass burning, urban, and desert dust aerosols,
1210 *J. Geophys. Res.- Atmos.*, 104, 31333-31349, <https://doi.org/10.1029/1999JD900923>, 1999.

1211 Eck, T. F., Holben, B. N., Reid, J., Giles, D., Rivas, M., Singh, R. P., Tripathi, S., Bruegge, C.,
1212 Platnick, S., and Arnold, G.: Fog-and cloud-induced aerosol modification observed by the
1213 Aerosol Robotic Network (AERONET), *J. Geophys. Res.- Atmos.*, 117,
1214 <https://doi.org/10.1029/2011JD016839>, 2012.

1215 Ervens, B., Sorooshian, A., Aldhaif, A. M., Shingler, T., Crosbie, E., Ziemba, L., Campuzano-
1216 Jost, P., Jimenez, J. L., and Wisthaler, A.: Is there an aerosol signature of chemical cloud
1217 processing?, *Atmos. Chem. Phys.*, 18, 16099-16119, <https://doi.org/10.5194/acp-18-16099-2018>,
1218 2018.

1219 Faloon, I.: Sulfur processing in the marine atmospheric boundary layer: A review and critical
1220 assessment of modeling uncertainties, *Atmos. Environ.*, 43, 2841-2854,
1221 <https://doi.org/10.1016/j.atmosenv.2009.02.043>, 2009.

1222 Feingold, G.: Modeling of the first indirect effect: Analysis of measurement requirements,
1223 *Geophys. Res. Lett.*, 30, <https://doi.org/10.1029/2003GL017967>, 2003.

1224 Flores, J.: Climate of the Philippines, *Climates of the Northern and Eastern Asia*, 159-213, 1969.

1225 Formenti, P., Andreae, M. O., and Lelieveld, J.: Measurements of aerosol optical depth above
1226 3570 m asl in the North Atlantic free troposphere: results from ACE-2, *Tellus B*, 52, 678-693,
1227 <https://doi.org/10.1034/j.1600-0889.2000.00006.x>, 2000.

1228 Garay, M. J., Bull, M. A., Nastan, A. M., Witek, M. L., Seidel, F. C., Diner, D. J., Kahn, R. A.,
1229 Limbacher, J. A., and Kalashnikova, O. V.: Data Product Specification for the MISR Level 2
1230 Aerosol Product, Jet Propulsion Laboratory, California Institute of Technology. JPL D-100649.
1231 https://asdc.larc.nasa.gov/documents/misr/DPS_AEROSOL_V023.20180125.pdf, 2018.

1232 Gautam, R., Hsu, N. C., Eck, T. F., Holben, B. N., Janjai, S., Jantarach, T., Tsay, S.-C., and Lau,
1233 W. K.: Characterization of aerosols over the Indochina peninsula from satellite-surface
1234 observations during biomass burning pre-monsoon season, *Atmos. Environ.*, 78, 51-59,
1235 <https://doi.org/10.1016/j.atmosenv.2012.05.038>, 2013.

1236 Gelaro, R., McCarty, W., Suárez, M. J., Todling, R., Molod, A., Takacs, L., Randles, C. A.,
1237 Darmenov, A., Bosilovich, M. G., and Reichle, R.: The modern-era retrospective analysis for
1238 research and applications, version 2 (MERRA-2), *J. Climate*, 30, 5419-5454,
1239 <https://doi.org/10.1175/JCLI-D-16-0758.1>, 2017.

1240 Geng, H., Hwang, H., Liu, X., Dong, S., and Ro, C.-U.: Investigation of aged aerosols in size-
1241 resolved Asian dust storm particles transported from Beijing, China, to Incheon, Korea, using
1242 low-Z particle EPMA, *Atmos. Chem. Phys.*, 14, 3307-3323, <https://doi.org/10.5194/acp-14-3307-2014>,
1243 2014.

- 1244 Giles, D. M., Holben, B. N., Eck, T. F., Sinyuk, A., Smirnov, A., Slutsker, I., Dickerson, R.,
 1245 Thompson, A., and Schafer, J.: An analysis of AERONET aerosol absorption properties and
 1246 classifications representative of aerosol source regions, *J. Geophys. Res.- Atmos.*, 117,
 1247 <https://doi.org/10.1029/2012JD018127>, 2012.
- 1248 Giles, D. M., Sinyuk, A., Sorokin, M. G., Schafer, J. S., Smirnov, A., Slutsker, I., Eck, T. F.,
 1249 Holben, B. N., Lewis, J. R., and Campbell, J. R.: Advancements in the Aerosol Robotic Network
 1250 (AERONET) Version 3 database—automated near-real-time quality control algorithm with
 1251 improved cloud screening for Sun photometer aerosol optical depth (AOD) measurements,
 1252 *Atmos. Meas. Tech.*, 12, 169-209, <https://doi.org/10.5194/amt-12-169-2019>, 2019.
- 1253 Glover, D., and Jessup, T.: The Indonesian fires and haze of 1997: the economic toll, *Economy
 1254 and Environment Program for SE Asia (EEPSEA) Singapore and the World Wildlife Fund
 1255 (WWF) Indonesia*, Jakarta, 1998.
- 1256 Guyon, P., Boucher, O., Graham, B., Beck, J., Mayol-Bracero, O. L., Roberts, G. C., Maenhaut,
 1257 W., Artaxo, P., and Andreae, M. O.: Refractive index of aerosol particles over the Amazon
 1258 tropical forest during LBA-EUSTACH 1999, *J. Aerosol Sci.*, 34, 883-907,
 1259 [https://doi.org/10.1016/S0021-8502\(03\)00052-1](https://doi.org/10.1016/S0021-8502(03)00052-1), 2003.
- 1260 Hartley, W. S., and Hobbs, P. V.: An aerosol model and aerosol-induced changes in the clear-sky
 1261 albedo off the east coast of the United States, *J. Geophys. Res.- Atmos.*, 106, 9733-9748,
 1262 <https://doi.org/10.1029/2001JD900025>, 2001.
- 1263 Haywood, J., and Boucher, O.: Estimates of the direct and indirect radiative forcing due to
 1264 tropospheric aerosols: A review, *Rev. Geophys.*, 38, 513-543,
 1265 <https://doi.org/10.1029/1999RG000078>, 2000.
- 1266 Hendrickson, B. N., Brooks, S. D., Thornton, D. C., Moore, R. H., Crosbie, E., Ziemba, L. D.,
 1267 Carlson, C. A., Baetge, N., Mirrielees, J. A., and Alsante, A. N.: Role of sea surface microlayer
 1268 properties in cloud formation, *Frontiers in Marine Science*, 7, 596225,
 1269 <https://doi.org/10.3389/fmars.2020.596225>, 2021.
- 1270 Herber, A., Thomason, L. W., Gernandt, H., Leiterer, U., Nagel, D., Schulz, K. H., Kaptur, J.,
 1271 Albrecht, T., and Notholt, J.: Continuous day and night aerosol optical depth observations in the
 1272 Arctic between 1991 and 1999, *J. Geophys. Res.- Atmos.*, 107, AAC 6-1-AAC 6-13,
 1273 <https://doi.org/10.1029/2001JD000536>, 2002.
- 1274 Hilario, M. R. A., Cruz, M. T., Bañaga, P. A., Betito, G., Braun, R. A., Stahl, C., Cambaliza, M.
 1275 O., Lorenzo, G. R., MacDonald, A. B., AzadiAghdam, M., Pabroa, P. C., Yee, J. R., Simpas, J.
 1276 B., and Sorooshian, A.: Characterizing weekly cycles of particulate matter in a coastal megacity:
 1277 The importance of a seasonal, size-resolved, and chemically-speciated analysis, *J. Geophys.
 1278 Res.- Atmos.*, 125, e2020JD032614, <https://doi.org/10.1029/2020JD032614>, 2020a.
- 1279 Hilario, M. R. A., Cruz, M. T., Cambaliza, M. O. L., Reid, J. S., Xian, P., Simpas, J. B.,
 1280 Lagrosas, N. D., Uy, S. N. Y., Cliff, S., and Zhao, Y.: Investigating size-segregated sources of

1281 elemental composition of particulate matter in the South China Sea during the 2011 Vasco
1282 cruise, *Atmos. Chem. Phys.*, 20, 1255-1276, <https://doi.org/10.5194/acp-20-1255-2020>, 2020b.

1283 Hilario, M. R. A., Crosbie, E., Shook, M., Reid, J. S., Cambaliza, M. O. L., Simpas, J. B. B.,
1284 Ziemba, L., DiGangi, J. P., Diskin, G. S., and Nguyen, P.: Measurement report: Long-range
1285 transport patterns into the tropical northwest Pacific during the CAMP 2 Ex aircraft campaign:
1286 chemical composition, size distributions, and the impact of convection, *Atmos. Chem. Phys.*, 21,
1287 3777-3802, <https://doi.org/10.5194/acp-21-3777-2021>, 2021a.

1288 Hilario, M. R. A., Olaguera, L. M., Narisma, G. T., and Matsumoto, J.: Diurnal characteristics of
1289 summer precipitation over Luzon Island, Philippines, *Asia-Pacific Journal of Atmospheric
1290 Sciences*, 57, 573-585, <https://doi.org/10.1007/s13143-020-00214-1>, 2021b.

1291 Hilario, M. R. A., Bañaga, P. A., Betito, G., Braun, R. A., Cambaliza, M. O., Cruz, M. T.,
1292 Lorenzo, G. R., MacDonald, A. B., Pabroa, P. C., and Simpas, J. B.: Stubborn aerosol: why
1293 particulate mass concentrations do not drop during the wet season in Metro Manila, Philippines,
1294 *Environmental Science: Atmospheres*, 2, 1428-1437, <https://doi.org/10.1039/D2EA00073C>,
1295 2022.

1296 Hogan, T. F., Liu, M., Ridout, J. A., Peng, M. S., Whitcomb, T. R., Ruston, B. C., Reynolds, C.
1297 A., Eckermann, S. D., Moskaitis, J. R., and Baker, N. L.: The navy global environmental model,
1298 *Oceanography*, 27, 116-125, <https://doi.org/10.5670/oceanog.2014.73>, 2014.

1299 Holben, B. N., Eck, T. F., Slutsker, I. a., Tanre, D., Buis, J., Setzer, A., Vermote, E., Reagan, J.
1300 A., Kaufman, Y., and Nakajima, T.: AERONET—A federated instrument network and data
1301 archive for aerosol characterization, *Remote Sens. Environ.*, 66, 1-16,
1302 [https://doi.org/10.1016/S0034-4257\(98\)00031-5](https://doi.org/10.1016/S0034-4257(98)00031-5), 1998.

1303 Holben, B. N., Tanre, D., Smirnov, A., Eck, T., Slutsker, I., Abuhassan, N., Newcomb, W.,
1304 Schafer, J., Chatenet, B., and Lavenu, F.: An emerging ground-based aerosol climatology:
1305 Aerosol optical depth from AERONET, *J. Geophys. Res.- Atmos.*, 106, 12067-12097,
1306 <https://doi.org/10.1029/2001JD900014>, 2001.

1307 Hong, Y., and Di Girolamo, L.: Cloud phase characteristics over Southeast Asia from A-Train
1308 satellite observations, *Atmos. Chem. Phys.*, 20, 8267-8291, [https://doi.org/10.5194/acp-20-8267-](https://doi.org/10.5194/acp-20-8267-2020)
1309 2020, 2020.

1310 Hong, Y., and Di Girolamo, L.: An overview of aerosol properties in clear and cloudy sky based
1311 on CALIPSO observations, *Earth and Space Science*, 9, e2022EA002287,
1312 <https://doi.org/10.1029/2022EA002287>, 2022.

1313 Hoppel, W., Frick, G., Fitzgerald, J., and Larson, R.: Marine boundary layer measurements of
1314 new particle formation and the effects nonprecipitating clouds have on aerosol size distribution,
1315 *J. Geophys. Res.- Atmos.*, 99, 14443-14459, <https://doi.org/10.1029/94JD00797>, 1994.

1316 Huang, C., Li, J., Sun, W., Chen, Q., Mao, Q.-J., and Yuan, Y.: Long-Term Variation
1317 Assessment of Aerosol Load and Dominant Types over Asia for Air Quality Studies Using

- 1318 Multi-Sources Aerosol Datasets, *Remote Sensing*, 13, 3116, <https://doi.org/10.3390/rs13163116>,
1319 2021.
- 1320 Hyer, E. J., Reid, J. S., Prins, E. M., Hoffman, J. P., Schmidt, C. C., Miettinen, J. I., and Giglio,
1321 L.: Patterns of fire activity over Indonesia and Malaysia from polar and geostationary satellite
1322 observations, *Atmos. Res.*, 122, 504-519, <https://doi.org/10.1016/j.atmosres.2012.06.011>, 2013.
- 1323 Jamora, J. B., Gudia, S. E. L., Go, A. W., Giduquio, M. B., and Loretero, M. E.: Potential CO2
1324 reduction and cost evaluation in use and transport of coal ash as cement replacement: A case in
1325 the Philippines, *Waste Manage.*, 103, 137-145, <https://doi.org/10.1016/j.wasman.2019.12.026>,
1326 2020.
- 1327 Jose, S., Gharai, B., Niranjana, K., and Rao, P.: Investigation on seasonal variations of aerosol
1328 properties and its influence on radiative effect over an urban location in central India, *Atmos.*
1329 *Environ.*, 133, 41-48, <https://doi.org/10.1016/j.atmosenv.2016.03.029>, 2016.
- 1330 Kaskaoutis, D., Kosmopoulos, P., Kambezidis, H., and Nastos, P.: Aerosol climatology and
1331 discrimination of different types over Athens, Greece, based on MODIS data, *Atmos. Environ.*,
1332 41, 7315-7329, <https://doi.org/10.1016/j.atmosenv.2007.05.017>, 2007.
- 1333 Kaskaoutis, D., Badarinath, K., Kumar Kharol, S., Rani Sharma, A., and Kambezidis, H.:
1334 Variations in the aerosol optical properties and types over the tropical urban site of Hyderabad,
1335 India, *Journal of Geophysical Research: Atmospheres*, 114,
1336 <https://doi.org/10.1029/2009JD012423>, 2009.
- 1337 Kiely, L., Spracklen, D. V., Wiedinmyer, C., Conibear, L., Reddington, C. L., Archer-Nicholls,
1338 S., Lowe, D., Arnold, S. R., Knute, C., and Khan, M. F.: New estimate of particulate emissions
1339 from Indonesian peat fires in 2015, *Atmospheric Chemistry and Physics*, 19, 11105-11121,
1340 <https://doi.org/10.5194/acp-19-11105-2019>, 2019.
- 1341 Kim, J.-S., and Park, K.: Atmospheric aging of Asian dust particles during long range transport,
1342 *Aerosol Sci. Tech.*, 46, 913-924, <https://doi.org/10.1080/02786826.2012.680984>, 2012.
- 1343 Kirchstetter, T. W., Novakov, T., and Hobbs, P. V.: Evidence that the spectral dependence of
1344 light absorption by aerosols is affected by organic carbon, *J. Geophys. Res.- Atmos.*, 109,
1345 <https://doi.org/10.1029/2004JD004999>, 2004.
- 1346 Koven, C. D., and Fung, I.: Inferring dust composition from wavelength-dependent absorption in
1347 Aerosol Robotic Network (AERONET) data, *J. Geophys. Res.- Atmos.*, 111,
1348 <https://doi.org/10.1029/2005JD006678>, 2006.
- 1349 Kudo, R., Nishizawa, T., and Aoyagi, T.: Vertical profiles of aerosol optical properties and the
1350 solar heating rate estimated by combining sky radiometer and lidar measurements, *Atmos. Meas.*
1351 *Tech.*, 9, 3223-3243, <https://doi.org/10.5194/amt-9-3223-2016>, 2016.
- 1352 Kumar, K. R., Sivakumar, V., Reddy, R. R., Gopal, K. R., and Adesina, A. J.: Identification and
1353 classification of different aerosol types over a subtropical rural site in Mpumalanga, South

- 1354 Africa: seasonal variations as retrieved from the AERONET Sunphotometer, *Aerosol Air Qual.*
1355 *Res.*, 14, 108-123, <https://doi.org/10.4209/aaqr.2013.03.0079>, 2014.
- 1356 Kumar, K. R., Yin, Y., Sivakumar, V., Kang, N., Yu, X., Diao, Y., Adesina, A. J., and Reddy,
1357 R.: Aerosol climatology and discrimination of aerosol types retrieved from MODIS, MISR and
1358 OMI over Durban (29.88 S, 31.02 E), South Africa, *Atmos. Environ.*, 117, 9-18,
1359 <https://doi.org/10.1016/j.atmosenv.2015.06.058>, 2015.
- 1360 Kuttippurath, J., and Raj, S.: Two decades of aerosol observations by AATSR, MISR, MODIS
1361 and MERRA-2 over India and Indian Ocean, *Remote Sens. Environ.*, 257, 112363,
1362 <https://doi.org/10.1016/j.rse.2021.112363>, 2021.
- 1363 Lee, H.-H., Iraqui, O., Gu, Y., Yim, S. H.-L., Chulakadabba, A., Tonks, A. Y.-M., Yang, Z., and
1364 Wang, C.: Impacts of air pollutants from fire and non-fire emissions on the regional air quality in
1365 Southeast Asia, *Atmos. Chem. Phys.*, 18, 6141-6156, <https://doi.org/10.5194/acp-18-6141-2018>,
1366 2018.
- 1367 Lee, J., Kim, J., Song, C., Kim, S., Chun, Y., Sohn, B., and Holben, B.: Characteristics of aerosol
1368 types from AERONET sunphotometer measurements, *Atmospheric Environment*, 44, 3110-
1369 3117, <https://doi.org/10.1016/j.atmosenv.2010.05.035>, 2010.
- 1370 Li, G., Bei, N., Cao, J., Huang, R., Wu, J., Feng, T., Wang, Y., Liu, S., Zhang, Q., and Tie, X.: A
1371 possible pathway for rapid growth of sulfate during haze days in China, *Atmos. Chem. Phys.*, 17,
1372 3301-3316, <https://doi.org/10.5194/acp-17-3301-2017>, 2017.
- 1373 Li, J., Carlson, B. E., and Lacis, A. A.: Application of spectral analysis techniques in the
1374 intercomparison of aerosol data: 1. An EOF approach to analyze the spatial-temporal variability
1375 of aerosol optical depth using multiple remote sensing data sets, *J. Geophys. Res.- Atmos.*, 118,
1376 8640-8648, <https://doi.org/10.1002/jgrd.50686>, 2013.
- 1377 Li, Z., Niu, F., Fan, J., Liu, Y., Rosenfeld, D., and Ding, Y.: Long-term impacts of aerosols on
1378 the vertical development of clouds and precipitation, *Nat. Geosci.*, 4, 888-894,
1379 <https://doi.org/10.1038/ngeo1313>, 2011.
- 1380 Lin, N.-H., Sayer, A. M., Wang, S.-H., Loftus, A. M., Hsiao, T.-C., Sheu, G.-R., Hsu, N. C.,
1381 Tsay, S.-C., and Chantara, S.: Interactions between biomass-burning aerosols and clouds over
1382 Southeast Asia: Current status, challenges, and perspectives, *Environ. Pollut.*, 195, 292-307,
1383 <https://doi.org/10.1016/j.envpol.2014.06.036>, 2014.
- 1384 Lloyd, S.: Least squares quantization in PCM, *IEEE T. Inform. Theory*, 28, 129-137,
1385 <https://doi.org/10.1109/TIT.1982.1056489>, 1982.
- 1386 Lynch, P., Reid, J. S., Westphal, D. L., Zhang, J., Hogan, T. F., Hyer, E. J., Curtis, C. A., Hegg,
1387 D. A., Shi, Y., and Campbell, J. R.: An 11-year global gridded aerosol optical thickness
1388 reanalysis (v1. 0) for atmospheric and climate sciences, *Geosci. Model Dev.*, 9,
1389 <https://doi.org/10.5194/gmd-9-1489-2016>, 2016.

- 1390 Matsumoto, J., Olaguera, L. M. P., Nguyen-Le, D., Kubota, H., and Villafuerte, M. Q.:
1391 Climatological seasonal changes of wind and rainfall in the Philippines, *Int. J. Climatol.*, 40,
1392 4843-4857, <https://doi.org/10.1002/joc.6492>, 2020.
- 1393 Moosmüller, H., and Sorensen, C.: Small and large particle limits of single scattering albedo for
1394 homogeneous, spherical particles, *J. Quant. Spectrosc. Ra.*, 204, 250-255,
1395 <https://doi.org/10.1016/j.jqsrt.2017.09.029>, 2018.
- 1396 Mora, M., Braun, R. A., Shingler, T., and Sorooshian, A.: Analysis of remotely sensed and
1397 surface data of aerosols and meteorology for the Mexico Megalopolis Area between 2003 and
1398 2015, *J. Geophys. Res.- Atmos.*, 122, 8705-8723, <https://doi.org/10.1002/2017JD026739>, 2017.
- 1399 Nakata, M., Mukai, S., and Yasumoto, M.: Seasonal and regional characteristics of aerosol
1400 pollution in east and southeast Asia, *Frontiers in Environmental Science*, 6, 29,
1401 <https://doi.org/10.3389/fenvs.2018.00029>, 2018.
- 1402 Fires and Smoke in Borneo: [https://earthobservatory.nasa.gov/images/40182/fires-and-smoke-in-](https://earthobservatory.nasa.gov/images/40182/fires-and-smoke-in-borneo)
1403 borneo), 2009.
- 1404 Nguyen, P., Shearer, E. J., Tran, H., Ombadi, M., Hayatbini, N., Palacios, T., Huynh, P.,
1405 Braithwaite, D., Updegraff, G., and Hsu, K.: The CHRS Data Portal, an easily accessible public
1406 repository for PERSIANN global satellite precipitation data, *Scientific Data*, 6, 1-10,
1407 <https://doi.org/10.1038/sdata.2018.296>, 2019a.
- 1408 Nguyen, T. T., Pham, H. V., Lasko, K., Bui, M. T., Laffly, D., Jourdan, A., and Bui, H. Q.:
1409 Spatiotemporal analysis of ground and satellite-based aerosol for air quality assessment in the
1410 Southeast Asia region, *Environmental Pollution*, 255, 113106,
1411 <https://doi.org/10.1016/j.envpol.2019.113106>, 2019b.
- 1412 North, G. R., Bell, T. L., Cahalan, R. F., and Moeng, F. J.: Sampling errors in the estimation of
1413 empirical orthogonal functions, *Mon. Weather Rev.*, 110, 699-706, [https://doi.org/10.1175/1520-](https://doi.org/10.1175/1520-0493(1982)110<0699:SEITEO>2.0.CO;2)
1414 0493(1982)110<0699:SEITEO>2.0.CO;2, 1982.
- 1415 O'Neill, N., Eck, T., Smirnov, A., Holben, B., and Thulasiraman, S.: Spectral discrimination of
1416 coarse and fine mode optical depth, *J. Geophys. Res.- Atmos.*, 108,
1417 <https://doi.org/10.1029/2002JD002975>, 2003.
- 1418 Oanh, N. K., Upadhyay, N., Zhuang, Y.-H., Hao, Z.-P., Murthy, D., Lestari, P., Villarin, J.,
1419 Chengchua, K., Co, H., and Dung, N.: Particulate air pollution in six Asian cities: Spatial and
1420 temporal distributions, and associated sources, *Atmospheric environment*, 40, 3367-3380,
1421 <https://doi.org/10.1016/j.atmosenv.2006.01.050>, 2006.
- 1422 Oanh, N. T. K., Permadi, D. A., Hopke, P. K., Smith, K. R., Dong, N. P., and Dang, A. N.:
1423 Annual emissions of air toxics emitted from crop residue open burning in Southeast Asia over
1424 the period of 2010–2015, *Atmos. Environ.*, 187, 163-173,
1425 <https://doi.org/10.1016/j.atmosenv.2018.05.061>, 2018.

- 1426 Ong, H. J. J., Lagrosas, N., Uy, S. N., Gacal, G. F. B., Dorado, S., Tobias Jr, V., and Holben, B.:
 1427 Determination of Monthly Aerosol Types in Manila Observatory and Notre Dame of Marbel
 1428 University from Aerosol Robotic Network (AERONET) measurements, AGU Fall Meeting
 1429 Abstracts, 2016, A54E-03,
- 1430 Pace, G., Sarra, A. d., Meloni, D., Piacentino, S., and Chamard, P.: Aerosol optical properties at
 1431 Lampedusa (Central Mediterranean). 1. Influence of transport and identification of different
 1432 aerosol types, *Atmos. Chem. Phys.*, 6, 697-713, <https://doi.org/10.5194/acp-6-697-2006>, 2006.
- 1433 Pandolfi, M., Alados-Arboledas, L., Alastuey, A., Andrade, M., Angelov, C., Artiñano, B.,
 1434 Backman, J., Baltensperger, U., Bonasoni, P., and Bukowiecki, N.: A European aerosol
 1435 phenomenology–6: scattering properties of atmospheric aerosol particles from 28 ACTRIS sites,
 1436 *Atmos. Chem. Phys.*, 18, 7877-7911, <https://doi.org/10.5194/acp-18-7877-2018>, 2018.
- 1437 Petters, M. D., Carrico, C. M., Kreidenweis, S. M., Prenni, A. J., DeMott, P. J., Collett Jr, J. L.,
 1438 and Moosmüller, H.: Cloud condensation nucleation activity of biomass burning aerosol, *J.*
 1439 *Geophys. Res.- Atmos.*, 114, <https://doi.org/10.1029/2009JD012353>, 2009.
- 1440 Plymale, N. T., Szekely, J. E., and Rubinstein, A. H.: Statistical Cluster Analysis of Global
 1441 Aerosol Optical Depth for Simplified Atmospheric Modeling, *J. Appl. Meteorol. Clim.*,
 1442 <https://doi.org/10.1175/JAMC-D-21-0150.1>, 2021.
- 1443 PSA: Highlights of the Philippine population 2015 census of population, Philippine Statistics
 1444 Authority, 2016.
- 1445 Qi, Y., Ge, J., and Huang, J.: Spatial and temporal distribution of MODIS and MISR aerosol
 1446 optical depth over northern China and comparison with AERONET, *Chinese science bulletin*,
 1447 58, 2497-2506, <https://doi.org/10.1007/s11434-013-5678-5>, 2013.
- 1448 Ramage, C. S.: Monsoon meteorology, Academic Press, New York, 1971.
- 1449 Randles, C., Da Silva, A., Buchard, V., Colarco, P., Darmenov, A., Govindaraju, R., Smirnov,
 1450 A., Holben, B., Ferrare, R., and Hair, J.: The MERRA-2 aerosol reanalysis, 1980 onward. Part I:
 1451 System description and data assimilation evaluation, *J. Climate*, 30, 6823-6850,
 1452 <https://doi.org/10.1175/JCLI-D-16-0609.1>, 2017.
- 1453 Reid, J., Koppmann, R., Eck, T., and Eleuterio, D.: A review of biomass burning emissions part
 1454 II: intensive physical properties of biomass burning particles, *Atmos. Chem. Phys.*, 5, 799-825,
 1455 <https://doi.org/10.5194/acp-5-799-2005>, 2005.
- 1456 Reid, J., Xian, P., Hyer, E., Flatau, M., Ramirez, E., Turk, F., Sampson, C., Zhang, C., Fukada,
 1457 E., and Maloney, E.: Multi-scale meteorological conceptual analysis of observed active fire
 1458 hotspot activity and smoke optical depth in the Maritime Continent, *Atmos. Chem. Phys.*, 12,
 1459 2117, <https://doi.org/10.5194/acp-12-2117-2012>, 2012.
- 1460 Reid, J., Maring, H., Narisma, G., van den Heever, S., Di Girolamo, L., Ferrare, R., Holz, R.,
 1461 Lawson, P., Mace, G., and Simpas, J.: The coupling between tropical meteorology, aerosol
 1462 lifecycle, convection, and radiation, during the Cloud, Aerosol and Monsoon Processes

1463 Philippines Experiment (CAMP 2 Ex), *B. Am. Meteorol. Soc.*, [https://doi.org/10.1175/BAMS-](https://doi.org/10.1175/BAMS-D-21-0285.1)
1464 [D-21-0285.1](https://doi.org/10.1175/BAMS-D-21-0285.1), 2023.

1465 Reid, J. S., Hobbs, P. V., Liou, S. C., Martins, J. V., Weiss, R. E., and Eck, T. F.: Comparisons
1466 of techniques for measuring shortwave absorption and black carbon content of aerosols from
1467 biomass burning in Brazil, *J. Geophys. Res.- Atmos.*, 103, 32031-32040,
1468 <https://doi.org/10.1029/98JD00773>, 1998.

1469 Reid, J. S., Hyer, E. J., Johnson, R. S., Holben, B. N., Yokelson, R. J., Zhang, J., Campbell, J. R.,
1470 Christopher, S. A., Di Girolamo, L., and Giglio, L.: Observing and understanding the Southeast
1471 Asian aerosol system by remote sensing: An initial review and analysis for the Seven Southeast
1472 Asian Studies (7SEAS) program, *Atmos. Res.*, 122, 403-468,
1473 <https://doi.org/10.1016/j.atmosres.2012.06.005>, 2013.

1474 Reid, J. S., Lagrosas, N. D., Jonsson, H. H., Reid, E. A., Sessions, W. R., Simpas, J. B., Uy, S.
1475 N., Boyd, T., Atwood, S. A., and Blake, D. R.: Observations of the temporal variability in
1476 aerosol properties and their relationships to meteorology in the summer monsoonal South China
1477 Sea/East Sea: the scale-dependent role of monsoonal flows, the Madden–Julian Oscillation,
1478 tropical cyclones, squall lines and cold pools, *Atmos. Chem. Phys.*, 15, 1745-1768,
1479 <https://doi.org/10.5194/acp-15-1745-2015>, 2015.

1480 Rizza, U., Mancinelli, E., Morichetti, M., Passerini, G., and Virgili, S.: Aerosol optical depth of
1481 the main aerosol species over Italian cities based on the NASA/MERRA-2 model reanalysis,
1482 *Atmosphere*, 10, 709, <https://doi.org/10.3390/atmos10110709>, 2019.

1483 Rolph, G., Stein, A., and Stunder, B.: Real-time environmental applications and display system:
1484 READY, *Environ. Modell. Softw.*, 95, 210-228, <https://doi.org/10.1016/j.envsoft.2017.06.025>,
1485 2017.

1486 Ross, J. L., Hobbs, P. V., and Holben, B.: Radiative characteristics of regional hazes dominated
1487 by smoke from biomass burning in Brazil: Closure tests and direct radiative forcing, *J. Geophys.*
1488 *Res.- Atmos.*, 103, 31925-31941, <https://doi.org/10.1029/97JD03677>, 1998.

1489 Saleh, R., Hennigan, C., McMeeking, G., Chuang, W., Robinson, E., Coe, H., Donahue, N., and
1490 Robinson, A.: Absorptivity of brown carbon in fresh and photo-chemically aged biomass-
1491 burning emissions, *Atmos. Chem. Phys.*, 13, 7683-7693, [https://doi.org/10.5194/acp-13-7683-](https://doi.org/10.5194/acp-13-7683-2013)
1492 [2013](https://doi.org/10.5194/acp-13-7683-2013), 2013.

1493 Schlosser, J. S., Braun, R. A., Bradley, T., Dadashazar, H., MacDonald, A. B., Aldhaif, A. A.,
1494 Aghdam, M. A., Mardi, A. H., Xian, P., and Sorooshian, A.: Analysis of aerosol composition
1495 data for western United States wildfires between 2005 and 2015: Dust emissions, chloride
1496 depletion, and most enhanced aerosol constituents, *J. Geophys. Res.- Atmos.*, 122, 8951-8966,
1497 <https://doi.org/10.1002/2017JD026547>, 2017.

1498 Schuster, G., Dubovik, O., and Arola, A.: Remote sensing of soot carbon—Part 1: Distinguishing
1499 different absorbing aerosol species, *Atmos. Chem. Phys.*, 16, 1565-1585,
1500 <https://doi.org/10.5194/acp-16-1565-2016>, 2016.

1501 Schuster, G. L., Dubovik, O., and Holben, B. N.: Angstrom exponent and bimodal aerosol size
1502 distributions, *J. Geophys. Res.- Atmos.*, 111, <https://doi.org/10.1029/2005JD006328>, 2006.

1503 Sharma, M., Kaskaoutis, D. G., Singh, R. P., and Singh, S.: Seasonal variability of atmospheric
1504 aerosol parameters over Greater Noida using ground sunphotometer observations, *Aerosol Air*
1505 *Qual. Res.*, 14, 608-622, <https://doi.org/10.4209/aaqr.2013.06.0219>, 2014.

1506 Shen, Z., Liu, J., Horowitz, L., Henze, D., Fan, S., Mauzerall, D. L., Lin, J.-T., and Tao, S.:
1507 Analysis of transpacific transport of black carbon during HIPPO-3: implications for black carbon
1508 aging, *Atmos. Chem. Phys.*, 14, 6315-6327, <https://doi.org/10.5194/acp-14-6315-2014>, 2014.

1509 Sinyuk, A., Holben, B. N., Eck, T. F., Giles, D. M., Slutsker, I., Korkin, S., Schafer, J. S.,
1510 Smirnov, A., Sorokin, M., and Lyapustin, A.: The AERONET Version 3 aerosol retrieval
1511 algorithm, associated uncertainties and comparisons to Version 2, *Atmospheric Measurement*
1512 *Techniques*, 13, 3375-3411, <https://doi.org/10.5194/amt-13-3375-2020>, 2020.

1513 Smirnov, A., Holben, B. N., Dubovik, O., O'Neill, N. T., Eck, T. F., Westphal, D. L., Gorocho, A.
1514 K., Pietras, C., and Slutsker, I.: Atmospheric aerosol optical properties in the Persian Gulf, *J.*
1515 *Atmos. Sci.*, 59, 620-634, [https://doi.org/10.1175/1520-](https://doi.org/10.1175/1520-0469(2002)059<0620:AAOPIT>2.0.CO;2)
1516 [0469\(2002\)059<0620:AAOPIT>2.0.CO;2](https://doi.org/10.1175/1520-0469(2002)059<0620:AAOPIT>2.0.CO;2), 2002.

1517 Smith, S. J., Aardenne, J. v., Klimont, Z., Andres, R. J., Volke, A., and Delgado Arias, S.:
1518 Anthropogenic sulfur dioxide emissions: 1850–2005, *Atmos. Chem. Phys.*, 11, 1101-1116,
1519 <https://doi.org/10.5194/acp-11-1101-2011>, 2011.

1520 Sorooshian, A., Wang, Z., Feingold, G., and L'Ecuyer, T. S.: A satellite perspective on cloud
1521 water to rain water conversion rates and relationships with environmental conditions, *J.*
1522 *Geophys. Res.- Atmos.*, 118, 6643-6650, <https://doi.org/10.1002/jgrd.50523>, 2013.

1523 Stahl, C., Cruz, M. T., Bañaga, P. A., Betito, G., Braun, R. A., Aghdam, M. A., Cambaliza, M.
1524 O., Lorenzo, G. R., MacDonald, A. B., and Hilario, M. R. A.: Sources and characteristics of size-
1525 resolved particulate organic acids and methanesulfonate in a coastal megacity: Manila,
1526 Philippines, *Atmos. Chem. Phys.*, 20, 15907-15935, <https://doi.org/10.5194/acp-20-15907-2020>,
1527 2020.

1528 Stahl, C., Crosbie, E., Bañaga, P. A., Betito, G., Braun, R. A., Cainglet, Z. M., Cambaliza, M. O.,
1529 Cruz, M. T., Dado, J. M., and Hilario, M. R. A.: Total organic carbon and the contribution from
1530 speciated organics in cloud water: airborne data analysis from the CAMP 2 Ex field campaign,
1531 *Atmos. Chem. Phys.*, 21, 14109-14129, <https://doi.org/10.5194/acp-21-14109-2021>, 2021.

1532 Stein, A., Draxler, R. R., Rolph, G. D., Stunder, B. J., Cohen, M., and Ngan, F.: NOAA's
1533 HYSPLIT atmospheric transport and dispersion modeling system, *B. Am. Meteorol. Soc.*, 96,
1534 2059-2077, <https://doi.org/10.1175/BAMS-D-14-00110.1>, 2015.

1535 Stevens, B., and Feingold, G.: Untangling aerosol effects on clouds and precipitation in a
1536 buffered system, *Nature*, 461, 607-613, <https://doi.org/10.1038/nature08281>, 2009.

- 1537 Sullivan, R. C., Levy, R. C., da Silva, A. M., and Pryor, S. C.: Developing and diagnosing
1538 climate change indicators of regional aerosol optical properties, *Scientific Reports*, 7, 1-13,
1539 <https://doi.org/10.1038/s41598-017-18402-x>, 2017.
- 1540 Tao, W. K., Chen, J. P., Li, Z., Wang, C., and Zhang, C.: Impact of aerosols on convective
1541 clouds and precipitation, *Rev. Geophys.*, 50, <https://doi.org/10.1029/2011RG000369>, 2012.
- 1542 Tsay, S.-C., Hsu, N. C., Lau, W. K.-M., Li, C., Gabriel, P. M., Ji, Q., Holben, B. N., Welton, E.
1543 J., Nguyen, A. X., and Janjai, S.: From BASE-ASIA toward 7-SEAS: A satellite-surface
1544 perspective of boreal spring biomass-burning aerosols and clouds in Southeast Asia,
1545 *Atmospheric environment*, 78, 20-34, <https://doi.org/10.1016/j.atmosenv.2012.12.013>, 2013.
- 1546 Van Beelen, A., Roelofs, G., Hasekamp, O., Henzing, J., and Röckmann, T.: Estimation of
1547 aerosol water and chemical composition from AERONET Sun–sky radiometer measurements at
1548 Cabauw, the Netherlands, *Atmos. Chem. Phys.*, 14, 5969-5987, <https://doi.org/10.5194/acp-14-5969-2014>, 2014.
- 1550 Wall, C. J., Norris, J. R., Possner, A., McCoy, D. T., McCoy, I. L., and Lutsko, N. J.: Assessing
1551 effective radiative forcing from aerosol–cloud interactions over the global ocean, *Proceedings of*
1552 *the National Academy of Sciences*, 119, e2210481119,
1553 <https://doi.org/10.1073/pnas.2210481119>, 2022.
- 1554 Wang, L., Lau, K.-H., Fung, C.-H., and Gan, J.-P.: The relative vorticity of ocean surface winds
1555 from the QuikSCAT satellite and its effects on the geneses of tropical cyclones in the South
1556 China Sea, *Tellus A*, 59, 562-569, <https://doi.org/10.1111/j.1600-0870.2007.00249.x>, 2007.
- 1557 Wang, S.-H., Welton, E. J., Holben, B. N., Tsay, S.-C., Lin, N.-H., Giles, D., Stewart, S. A.,
1558 Janjai, S., Nguyen, X. A., and Hsiao, T.-C.: Vertical distribution and columnar optical properties
1559 of springtime biomass-burning aerosols over Northern Indochina during 2014 7-SEAS
1560 campaign, *Aerosol and Air Quality Research*, 15, 2037-2050,
1561 <https://doi.org/10.4209/aaqr.2015.05.0310>, 2015.
- 1562 Wu, M.-c., and Choy, C.-w.: An Observational Study of the Changes in the Intensity and Motion
1563 of Tropical Cyclones crossing Luzon, *Tropical Cyclone Research and Review*, 4, 95-109,
1564 <https://doi.org/10.6057/2015TCRRh3.01>, 2016.
- 1565 Xian, P., Reid, J. S., Atwood, S. A., Johnson, R. S., Hyer, E. J., Westphal, D. L., and Sessions,
1566 W.: Smoke aerosol transport patterns over the Maritime Continent, *Atmos. Res.*, 122, 469-485,
1567 <https://doi.org/10.1016/j.atmosres.2012.05.006>, 2013.
- 1568 Xiao, N., Shi, T., Calder, C. A., Munroe, D. K., Berrett, C., Wolfenbarger, S., and Li, D.: Spatial
1569 characteristics of the difference between MISR and MODIS aerosol optical depth retrievals over
1570 mainland Southeast Asia, *Remote Sensing of Environment*, 113, 1-9,
1571 <https://doi.org/10.1016/j.rse.2008.07.011>, 2009.
- 1572 Xie, Y., Li, Z., Zhang, Y., Zhang, Y., Li, D., Li, K., Xu, H., Zhang, Y., Wang, Y., and Chen, X.:
1573 Estimation of atmospheric aerosol composition from ground-based remote sensing

- 1574 measurements of Sun-sky radiometer, *J. Geophys. Res.- Atmos.*, 122, 498-518,
1575 <https://doi.org/10.1002/2016JD025839>, 2017.
- 1576 Yang, S., Lau, W. K., Ji, Z., Dong, W., and Yang, S.: Impacts of radiative effect of pre-monsoon
1577 biomass burning aerosols on atmospheric circulation and rainfall over Southeast Asia and
1578 southern China, *Climate Dynamics*, 59, 417-432, <https://doi.org/10.1007/s00382-021-06135-7>,
1579 2022.
- 1580 Yumul Jr, G. P., Cruz, N. A., Dimalanta, C. B., Servando, N. T., and Hilario, F. D.: The 2007 dry
1581 spell in Luzon (Philippines): its cause, impact and corresponding response measures, *Climatic
1582 change*, 100, 633-644, <https://doi.org/10.1007/s10584-009-9677-0>, 2010.
- 1583 Zhao, G., Di Girolamo, L., Dey, S., Jones, A. L., and Bull, M.: Examination of direct cumulus
1584 contamination on MISR-retrieved aerosol optical depth and angstrom coefficient over ocean,
1585 *Geophysical Research Letters*, 36, <https://doi.org/10.1029/2009GL038549>, 2009.
- 1586 Zhao, G., Zhao, C., Kuang, Y., Bian, Y., Tao, J., Shen, C., and Yu, Y.: Calculating the aerosol
1587 asymmetry factor based on measurements from the humidified nephelometer system, *Atmos.
1588 Chem. Phys.*, 18, 9049-9060, <https://doi.org/10.5194/acp-18-9049-2018>, 2018.